Spring 2004

Optimization studies of thermal bimorph cantilevers, electrostatic torsion actuators and variable capacitors

Wuyong Peng
New Jersey Institute of Technology

ABSTRACT

OPTIMIZATION STUDIES OF THERMAL BIMORPH CANTILEVERS, ELECTROSTATIC TORSION ACTUATORS AND VARIABLE CAPACITORS

by
Wuyong Peng

In this dissertation, theoretical analyses and optimization studies are given for three kinds of MEMS devices: thermal bimorph cantilevers, electrostatic torsion actuators, and variable capacitors. Calculation, simulation, and experimental data are used to confirm the device behavior and demonstrate the application of the design approaches.

For thermal bimorph cantilevers, an analytical model is presented which allows theoretical analysis and quantitative optimization of the performance based on material properties and device dimensions. Bimorph cantilevers are divided into two categories for deflection optimization: either the total thickness is constant, or the cantilever has one constant and one variable layer thickness. The optimum equations are then derived for each case and can be used as design rules. The results show that substantial improvements are possible over existing design approaches. Other parameters like static temperature distribution, power consumption, and dynamic behavior are also discussed, as are design tradeoffs such as feature size, application constraints, fabrication feasibility, and cost.

The electrostatic torsion actuator studies are conducted for two device types: round and rectangular. The first case describes an analytical study of the pull-in effect in round, double-gimbaled, electrostatic torsion actuators with buried, variable length electrodes, designed for optical cross-connect applications. It is found that the fractional tilt at pull-in for the inner round plate in this system depends only on the ratio of the length of the buried electrode to the radius of the plate. The fractional tilt at pull-in for the

outer support ring depends only on the ratio of the length of the buried electrode to the outer radius of the ring and the ratio of the ring's inner and outer radii. Expressions for the pull-in voltage are determined in both cases. General relationships are also derived relating the applied voltage to the resulting tilt angle, both normalized by their pull-in values. Calculated results are verified by comparison with finite element MEMCAD simulations, with fractional difference smaller than 4% for torsion mode dominant systems. For the second case, a fast, angle based design approach for rectangular electrostatic torsion actuators based on several simple equations is developed. This approach is significantly more straightforward than the usual full calculation or simulation methods. The main results of the simplified approach are verified by comparing them with analytical calculations and MEMCAD simulations with fractional difference smaller than 3% for torsion mode dominant actuators. Also, good agreement is found by comparison with the measured behavior of a micro-fabricated full-plate device.

In the last topic, ultra-thin silicon wafers, SU-8 bonding and deep reactive ion etching technology have been combined for the fabrication of folded spring, dual electrostatic drive, vertical plate variable capacitor devices with displacement limiting bumpers. Due to the presence of the bumpers, the variable capacitor with parallel plate drive electrodes has two tuning voltage regimes: first a parabolic region that achieves roughly a 290% tuning range, then a linear region that achieves an additional 310%, making the total tuning range about 600%. The variable capacitor with comb drive electrodes has a parabolic region that achieves roughly a 205% tuning range, then a linear region that achieves an additional 37%, making its total tuning range about 242%. The variable capacitors have Q factors around 100 owing to the use of silicon electrodes other than lower resistivity metal.

OPTIMIZATION STUDIES OF THERMAL BIMORPH CANTILEVERS, ELECTROSTATIC TORSION ACTUATORS AND VARIABLE CAPACITORS

by

Wuyong Peng

A Dissertation
Submitted to the Faculty of
New Jersey Institute of Technology
In Partial Fulfillment of the Requirements for the Degree of
Doctor of Philosophy in Materials Science and Engineering

Interdisciplinary Program in Materials Science and Engineering

May 2004

APPROVAL PAGE

OPTIMIZATION STUDIES OF THERMAL BIMORPH CANTILEVER, ELECTROSTATIC TORSION ACTUATOR, AND VARIABLE CAPACITOR

Wuyong Peng

Dr. Kenneth.R. Farmer, Dissertation Advisor — Date
Associate Professor of Physics, NJIT

Dr. Durgamadhab Misra, Co-Advisor — Date
Professor of Electrical and Computer Engineering, NJIT

Dr. Ken K Chin, Committee Member — Date
Professor of Physics, NJIT

Dr. Zhixiong Xiao, Committee Member — Date
Assistant Research Professor of Physics, NJIT

Dr. Baoqing Li, Committee Member — Date
Senior Research Specialist of Physics, NJIT

BIOGRAPHICAL SKETCH

Author: Wuyong Peng

Degree: Doctor of Philosophy

Date: May 2004

Undergraduate and Graduate Education:

- Doctor of Philosophy in Materials Science and Engineering,
  New Jersey Institute of Technology, Newark, NJ, 2004

- Master of Science in Electrical and Computer Engineering,
  New Jersey Institute of Technology, Newark, NJ, 2004

- Bachelor of Science in Materials Science,
  Zhejiang University, Hangzhou, P. R. China, 1993

Major: Materials Science and Engineering

Presentations and Publications:

Z. Xiao, W. Peng, and K. R. Farmer,
"Analytical behavior of rectangular electrostatic torsion actuators with nonlinear spring bending",
Journal of Microelectromechanical Systems, vol. 12, pp. 929-936, 2003.

W. Peng, Z. Xiao, and K. R. Farmer,
"Optimization of thermally actuated bimorph cantilevers for maximum deflection",
Proceedings of Nanotech 2003, San Francisco, CA, vol. 1, pp. 376-379, 2003.

Z. Xiao, W. Peng, R. F. Wolffenbuttel, and K. R. Farmer,
"Micromachined variable capacitor with wide tuning range",
Proceedings of Solid-State Sensor, Actuator and Microsystems Workshop, Hilton Head Island, SC, pp. 346-349, 2002.

Z. Xiao, W. Peng, X. Wu, and K. R. Farmer,
"Pull-in study for round double-gimbaled electrostatic torsion actuators",
J. Micromech. Microeng. vol. 12, pp. 77-81, 2002.

Z. Xiao, X. Wu, W. Peng, and K. R. Farmer,
"An angle-based design approach for rectangular electrostatic torsion actuators",
Journal of Microelectromechanical Systems, vol. 10, pp. 561-568, 2001.

To my beloved family

ACKNOWLEDGMENT

I would like to express my deepest appreciation to my advisor, Dr. Kenneth R. Farmer, II, for his constant support, guidance, encouragement, and patience. Special thanks go to Dr. Durgamadhab Misra and Dr. Ken K. Chin for their valuable comments.

I would like to thank Dr. Zhixiong Xiao, Dr. Baoqing Li and other graduate fellows for helpful discussions and suggestions during the study.

Finally, I would like to thank my parents and my sister for their unconditional support for all these years.

TABLE OF CONTENTS

TABLE OF CONTENTS
(Continued)

Chapter **Page**

LIST OF TABLES

LIST OF FIGURES

LIST OF FIGURES
(Continued)

LIST OF FIGURES
(Continued)

CHAPTER 1

INTRODUCTION

For the last few decades, MEMS (Micro-Electro-Mechanical Systems) technology has been used in many application areas such as optics, communications, sensors, fluids and biology [1-15]. In optical areas devices like scanners, display units, projectors, micro mirrors, optical switches, spectrometers, tunable filters, gas detectors, micro lens, gratings, waveguides, photo diodes and other optoelectronic components are used to deflect, switch, or modulate an optical beam. In RF and wireless communications, MEMS has been used to make variable capacitors, inductors, transmitters and receivers. MEMS pressure sensors, accelerometers, gyroscopes and humidity sensors are well known in the sensors area. In microfluidic applications, MEMS has been used to make printer heads, fluid meters, micro pumps and fuel cells. Furthermore, MEMS devices are also used in medical areas for DNA analysis, disease diagnosis and even artificial retinas for the blind.

The core technology of MEMS is derived from the planar lithographic technologies of integrated circuits with additional processes that permit the fabrication of mechanical, optical, magnetic, acoustic, electronic and other components to sense, amplify, digitize, process signals and provide useful reaction output. The ultimate goal is to integrate all necessary functions in one module and realize SOC (Systems on Chip). The most noticeable benefit of MEMS devices compared to their classical macroscopic counterparts is the size reduction: many rigid materials become flexible in micro dimensions. And with the use of single-crystal material, fatigue phenomenon is less of a

problem due to the absence of grain boundaries. Other advantages include increased speed, lower power consumption, increased reliability, better performance, lower cost, etc. This is a rich field of research and development in which some applications have already reached the commercial level and other show a promising future.

The actuating mechanisms that have been used in MEMS devices include: electrostatic, piezoelectric, magnetic, and thermal actuation [16-18]. The most common actuation mechanism in MEMS is electrostatic because of its straightforward principle, compatibility with CMOS processes and materials, and relatively low consumption of power. Disadvantages include potentially high driving voltage and non-linear voltage response. In piezoelectric actuation, the electrically induced strain is approximately proportional to the applied electric field. Its advantages include large force, fast response time, and potentially low operating voltage. Disadvantages include small dimensional variations and a need for a sophisticated fabrication process. There are many advantages of using magnetic actuation (electromagnetic or magnetostrictive). For example, magnetic forces can be both attractive and repulsive. They are large in magnitude and effective over a long range. The major disadvantage of magnetic actuation is the lack of mature fabrication technology. This is mainly because it requires more complicated components, such as coils and magnetic materials. Thermal actuation provides large force and deflection. It has the advantages of low driving voltage and a nearly linear deflection-versus-power relationship. Thermally actuated device processes are often based on fairly straightforward fabrication steps and can be easily integrated with circuitry using, for example, a standard CMOS process. Disadvantages include high power consumption and comparatively long response time. Other actuation mechanisms include Shape Memory

Alloy (SMA) actuation, chemical reaction actuation, or a combination of two or more of any of the previously discussed mechanisms. Each may have a particular specialized application area. In summary, there are many actuation mechanisms to choose from that can be used in MEMS. None has dominance over the others: some are better in certain areas, some are mature and some promise potential benefits. The choice is a balance between many factors, such as design specifications, application constraints, process compatibility and cost. Table 1.1 is a brief comparison of the different actuation mechanisms.

Table 1.1 A brief comparison of actuation mechanisms used in MEMS

Actuation Mechanism	Advantages	Disadvantages
Electrostatic	Straightforward principle CMOS compatible Less power	High driving voltage Nonlinear response
Piezoelectric	Large force Short response time Low driving voltage	Sophisticated fabrication steps
Magnetic	Large force Effective over a long range Can be attractive or repulsive	Complicated components Needs magnetic materials No mature fabrication technology
Thermal	Large force and deflection Low driving voltage Linear deflection response with power Simple fabrication and IC compatible	High power consumption Long response time

Bimorph structures have long been studied and used for sensors and actuators because of their sensitivity, fast response time and ease of integration with semiconductor technology [19-21]. They can also provide important information about material properties such as residual stress, elastic modulus, piezoresistivity and magnetostriction [22-26]. Furthermore, bimorph structures have been found in almost all MEMS devices,

whether it is desired or not. Thus, the study of bimorph structures is of great interest either for better performance or to avoid unwanted effects. Traditionally, this is approached by numerical, simulation, or experimental methods [27-31]. Despite their wide use, the relationships between design parameters and device performance are still not clear. Several studies, however, have already addressed theoretical optimization of bimorph cantilevers [32-34], but theoretical solutions are only given for a specific case and cannot applied to other situations. Thus, a complete analysis for general bimorph cantilevers is needed. This study performs a thorough analysis of bimorph cantilevers driven by thermal stimulus. An analytical model is introduced, which allows theoretical analysis and quantitative optimization based on material properties and dimensions. The optimum equations are derived, which can be used as design rules. Further analysis shows that substantial improvements over existing design methods are possible with this optimization approach.

In response to the demand for increased information capacity, microelectromechanical systems (MEMS), including optical cross-connects, optical switches, and electrically controlled variable attenuators, are being investigated for the emerging all optical telecommunications network [63]. Electrostatic torsion actuators have been implemented in many of these optical MEMS systems. An important property of the actuators is their pull-in voltage, beyond which the electrostatic torque overcomes the mechanical torque, and the movable plate snaps abruptly to the fixed electrode plane. The aim of a typical design is to determine spring and electrode parameters for a chosen working point near pull-in that corresponds to a desired maximum controllable tilt angle at a given applied bias voltage. Numerous papers address rectangular torsion actuators

and the related pull-in voltage [64-73]. Among them, Hornbeck [69] uses an analysis based on the balance between the supporting beam torsion spring torque and the distributed 2-D electrostatic torque on the plate, but this approach does not lead to a straightforward expression for the pull-in voltage and the fractional deflection at the pull-in. Osterberg [70] and Gupta [71] have used electrostatically actuated microelectromechanical test structures for measurement of device and material properties, including pull-in. With this approach, Osterberg derives a 1-D lumped model equation for the spring constant of a rectangular torsion beam, and uses this expression in a pull-in voltage equation. However, the fractional deflection is not derived. Degani, et al., [72] have proposed polynomial algebraic equations for the pull-in voltage and angle in torsion actuators. However, this calculation is relatively complicated and time consuming, and must be repeated for every design variation. In this study, an angle based design approach for rectangular, electrostatic torsion actuators are proposed based on several straightforward equations. This approach makes the design optimization process much easier and faster than the usual full analytical calculation or finite element simulation methods. The results of the simplified approach are verified by comparing them with analytical calculations and MEMCAD simulations with fractional difference smaller than 3% for torsion mode dominant actuators. Also, the predicted results are compared with the measured behavior of a full-plate device, and found to be in good agreement. Moreover, for round, double-gimbaled, electrostatic torsion actuators with buried, variable length electrodes [63], the pull-in effect theory is still absent from the literature. The results of this study will be useful for optimizing the design of such actuators without the need for time-consuming finite element simulations.

Electronically tunable capacitors are key elements in communications circuits such as voltage-controlled oscillators and tunable capacitor filters. Numerous papers address variable capacitors [76-91]. In an integrated circuit design, a variable capacitor is usually realized with a reversed p-n junction, which can give a 335% tuning range [88]. However, the silicon p-n junction usually has large series resistance plus parasitic capacitance to the substrate. The variable capacitors manufactured with micromachining technology can accommodate large voltage swings so that the phase noise can be improved by allowing a large voltage swing across an LC circuit. This is normally not possible with p-n junction capacitors, where the designer must ensure that the junction does not become forward-biased over the tuning voltage range. Additionally, micro-mechanical capacitors are not expected to respond to microwave frequencies, which are normally 10,000 times higher than their mechanical resonant frequencies. For electrostatic drive variable capacitors fabricated using micromachining processes, Yao, et al., [88] have reported a capacitor with a tuning range of 200% based on lateral comb structures on an SOI substrate with a Q value of 34 at 500MHz. Feng, et al., [91] have used a thermal actuator in their variable capacitor and achieved a tuning range of 270% with Q values up to 290 at 1GHz. Borwick, et al., [92] achieved a variable capacitor with 740% using comb drive electrodes with Q values in excess of 100 in the 200-400 MHz range. In this study, ultra-thin silicon wafers, SU-8 bonding and deep reactive ion etching technology have been combined for the fabrication of folded spring, dual electrostatic drive, and vertical plate devices with displacement limiting bumpers. Both comb drive and parallel plate drive electrode structures have been fabricated and tested. The parallel plate driven devices exhibit a total tuning range of about 600%.

CHAPTER 2

THERMAL BIMORPH CANTILEVER

A bimorph cantilever is made up of two layers of materials with different physical properties and dimensions. One end of the structure is fixed; the other one is free of movement. A typical bimorph cantilever and its dimensions are defined in Figure 2.1. Where w_1, w_2; t_1, t_2 are the width and thickness of each layer, respectively, L is the length.

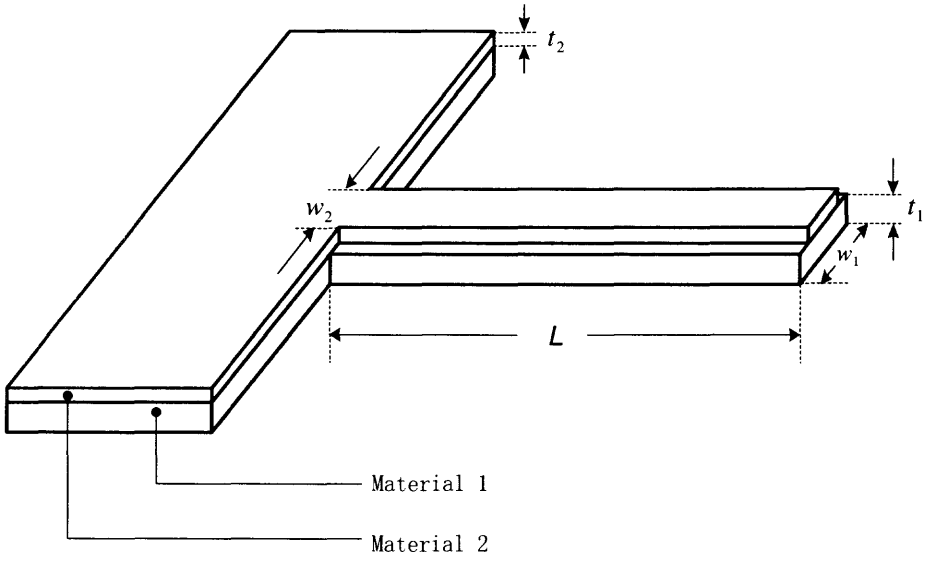

Figure2.1 A typical bimorph cantilever structure.

At its initial temperature (T_0), the cantilever is in a relaxed state: there is no stress within the cantilever and no deflection. When the temperature changes, the dimensions of these two layers will change differently due to different Thermal Expansion Coefficient (TEC). This small mismatch introduces a large stress in the interface. The stress is compressive in one layer and tensile in the other. Compressively stressed films tend to expand parallel to the substrate surface. Films in tensile stress, on the other hand, contract

parallel to the substrate. To release the stress, the cantilever will bend out of plane and the stress decreases with the deflection. On the other hand, part of the beam changes its stress state when bending and generates a counter force that increases with the deflection. When these two forces are balanced, the cantilever is in its equilibrium state again. The stress, and with it the force that can be generated by thermal expansion, are large, whereas the strain is small. Bimorph cantilevers can convert this small strain into relatively large out of plane displacement, as shown in Figure 2.2. The end of the cantilever is assumed to be a plane before and after deflection, which means that the linear stress distribution along the thickness of the cantilever and the resulting deflection are within the elastic limits for the materials.

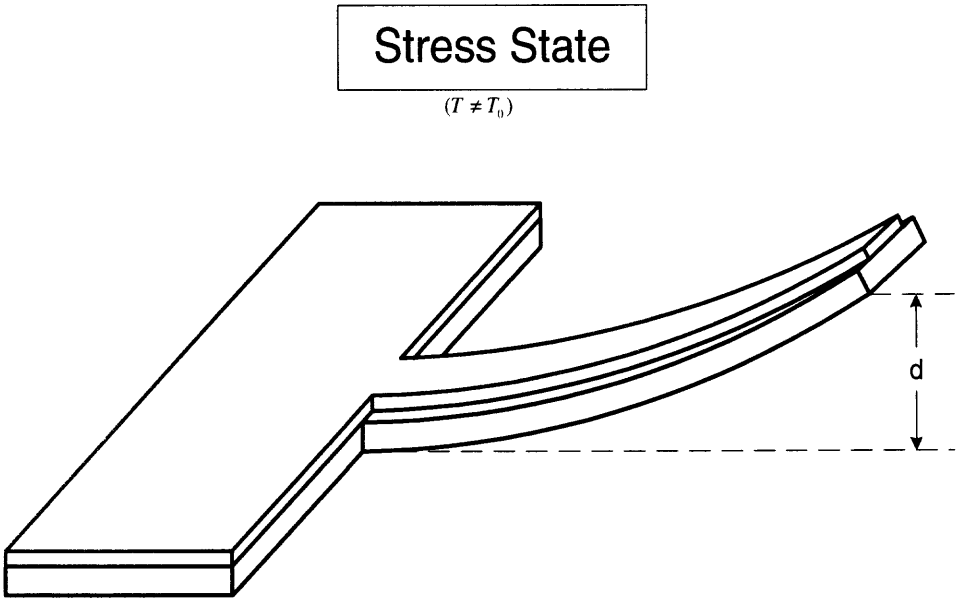

Figure 2.2 Deflecting of a bimorph cantilever due to temperature change.

2.1 Stress Analysis

2.1.1 Thermal Stress

For a free material layer, the strain created by thermal expansion can be expressed:

$$\varepsilon = \alpha \cdot \Delta T \tag{2.1}$$

where ε is the strain, α is the thermal expansion coefficient, and ΔT is the temperature change.

For an unreleased materials layer, according to Hook's Law ($\sigma = E \cdot \varepsilon$), the thermal stress is:

$$\sigma = E \cdot \alpha \cdot \Delta T \tag{2.2}$$

where σ is the stress and E is the Young's modulus. This equation shows that the stress generated by thermal expansion is independent of the dimensions of the device. Therefore, the corresponding force scales with the area as far as the material withstands the thermal stress.

Figure 2.3 represents the strain distribution within a thermal bimorph cantilever before and after release, T_0 indicates the initial state. When the temperature increases, both layers will elongate accordingly. Assume layer 2 has a larger thermal expansion coefficient than layer 1; it will try to expand more. Hence, layer 1 is in tensile stress and layer 2 is in compressive stress. Before the cantilever is released, an equilibrium position can be found by balancing the force:

$$\Sigma F = \int_{A_1} (\sigma_1 \cdot dA) + \int_{A_2} (\sigma_2 \cdot dA) = 0 \tag{2.3}$$

where σ_1 and σ_2 are the stress of each layer, A_1 and A_2 are the area.

Assume uniform stress distribution along the thickness, the equation is solved:

$$\Delta L = \frac{E_1' b_1 t_1 \alpha_1 + E_2' b_2 t_2 \alpha_2}{E_1' b_1 t_1 + E_2' b_2 t_2} \cdot \Delta T \cdot L_0 \tag{2.4}$$

where $E_1' = \frac{E_1}{1-\nu_1}$, $E_2' = \frac{E_2}{1-\nu_2}$ are the lateral Young's modulus and ν_1, ν_2 are the Poisson's ratio.

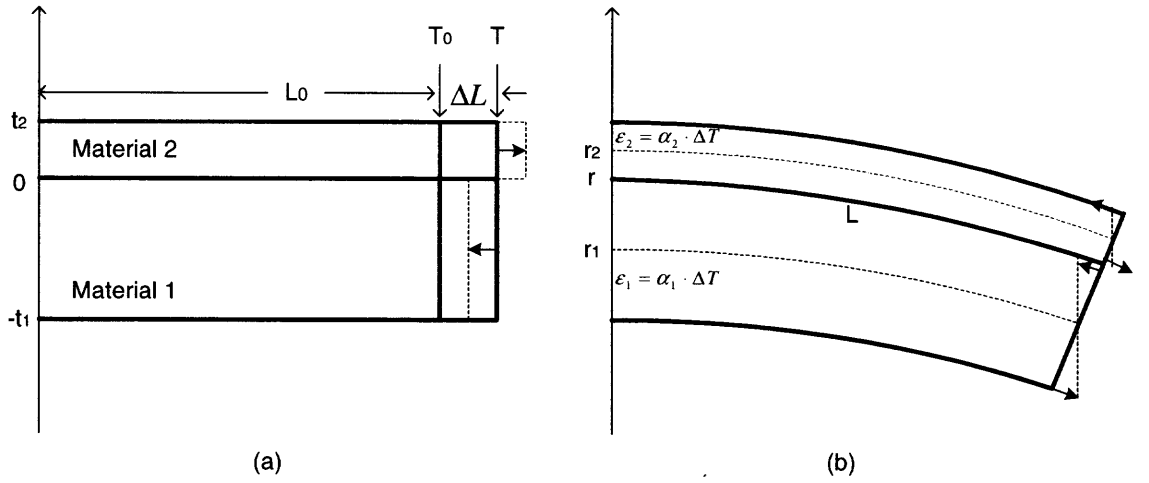

Figure 2.3 Strain distributions within a thermal bimorph cantilever before (a) and after (b) release. Note the existence of neutral planes after release.

Once the beam is released, due to the fact that layer 1 is in tensile stress and tends to shorten while layer 2 is in compressive stress and tends to elongate, the cantilever will bend down. Layer 1 will be partially compressed and tensed; the stress within it will change progressively from tension to compression. Hence, there exists a neutral plane where there is no stress. Similarly, the stress distribution in layer 2 changes from compression to tension, and there exists another neutral plane. The equilibrium state of the released cantilever is reached when the total force and the total bending moments are equal to zero:

$$\Sigma F = \int_{A_1} (\sigma_1 \cdot dA) + \int_{A_2} (\sigma_2 \cdot dA) = 0 \tag{2.5}$$

$$\Sigma M = \int_{A_1} (\sigma_1 \cdot t \cdot dA) + \int_{A_2} (\sigma_2 \cdot t \cdot dA) = 0 \tag{2.6}$$

Assume linear strain distribution along the thickness of the beam:

$$\varepsilon = \Delta\varepsilon - \frac{t}{r} \tag{2.7}$$

where $\Delta\varepsilon$ is the strain at the interface, and r is the radius of the cantilever.

From Equation 2.5 to 2.7, the curvature can be solved (Equation 2.8). Moreover, the positions of the two neutral planes and the stress distribution within each layer can also be derived. Of course, the neutral plane does not have to be within the layers. For example, if layer 2 is very thin and soft compared to layer 1, then after release it may still be compressed. In this case, the neutral plane moves out of the layer.

$$k = \frac{1}{r} = \frac{6w_1w_2E_1'E_2't_1t_2(t_1+t_2)\Delta\alpha\Delta T}{(w_1E_1't_1^2)^2 + (w_2E_2't_2^2)^2 + 2w_1w_2E_1'E_2't_1t_2(2t_1^2 + 3t_1t_2 + 2t_2^2)} \tag{2.8}$$

where w_1, w_2, t_1, t_2, E_1', E_2' are width, thickness and lateral Young's modulus of each material, respectively, $\Delta\alpha$ is the TEC difference of these two materials, and ΔT is the temperature change between the initial and working temperature. This model is based on the following assumptions:

- The deformation is within the elastic region of the materials,
- There is a linear strain distribution through the thickness of the cantilever,
- Materials are considered to be isotropic and uniform,
- There is no stress along the thickness direction,
- The temperature distribution is uniform over the whole beam, and
- Material properties remain constant.

To simplify Equation 2.8, define $t_2 / t_1 = x$, $w_2 / w_1 = y$ and $E_2'/E_1' = c$, the equation becomes:

$$k = \frac{1}{r} = \frac{cxy(1+x)^2}{c^2x^4y^2 + 4cx^3y + 6cx^2y + 4cxy + 1} \cdot \frac{6\Delta\alpha \cdot \Delta T}{t_1 + t_2} \tag{2.9}$$

This shows that the curvature is proportional to $\Delta\alpha$ and ΔT , and inversely proportional to the thickness. The effects of width and Young's modulus are reduced to relative values.

For future analysis, a bimorph cantilever driven by resistive heating is created in Figure 2.4. It is made up of Silicon and Aluminum, with a length of 500μm. The width and thickness of Silicon layer are 110μm and 5μm, respectively. The line width and spacing for the Aluminum resistor are each 10μm, corresponding to a total width of 60μm. The thickness is 2μm. Material properties of interest are listed in Table 2.1.

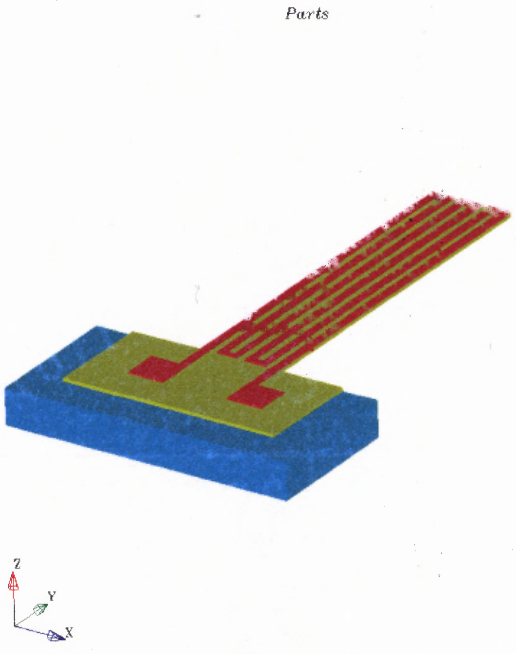

Figure 2.4 A thermal bimorph cantilever created for further analysis.

Table 2.1 Material properties at room temperature [36-38]

	Density (kg/m^3)	Young's Modulus (GPa)	Poisson's Ratio	TEC ($10^{-6}/K$)	Thermal Conductivity (W/m·K)	Heat Capacity (J/kg·K)	Electrical Resistivity (Ω·m)
Si	2330	169	0.3	2.6	148	705	2300
P-Si	2230	165	0.23	2.8	148	705	2300
SiO_2	2200	75	0.17	0.5	1.4	835	∞
Si_3N_4	3100	380	0.27	1.6	30.1	710	∞
Al	2700	70	0.35	23.1	237	898	2.655e-8
Au	19300	78	0.35	14.1	315	128	2.35e-8
Cr	7150	248	0.3	4.9	93.7	447	1.29e-7
Cu	8960	128	0.36	16.8	398	384	1.673e-8
Ni	8900	206	0.3	12.7	90.7	443	6.84e-8
Ti	4510	116	0.32	8.6	21.9	522	4.2e-7

2.1.2 Residual Stress

A common situation with many bimorph cantilevers is non-zero tip deflection (or curvature) at room temperature due to residual stress in the layers. Nearly all films are found to be in a state of residual internal stress, regardless of the means by which they have been produced. The stress may be compressive or tensile. Residual stresses are composed of thermal stress, resulting from deposition temperature conditions, and intrinsic stress, developed during the film nucleation. Intrinsic stresses are not yet completely understood. Several stress-causing mechanisms have been proposed: lattice mismatch between the substrate and the film, rapid film growth (which locks in defects), recrystallization processes, phase transformations and incorporation of impurities into the film [40, 41, 48]. Moreover, the stress values found in the literature should be considered representative rather than precise. Published data is often inconsistent, even if the investigators have employed similar measurement techniques. In general the intrinsic stress in a film depends on thickness, deposition rate, deposition temperature, ambient

pressure, method of film preparation, type of substrate used, type of machine used for fabrication, and a number of other parameters.

G. Lammel et al. [20] analyzed initial stress within bimorph cantilevers and showed that the curvature due to residual stress and the curvature due to thermal contributions are additive. Thus, for example, a zero deflection state can be attained by changing the temperature.

2.2 Deflection

The tip deflection of a thermal bimorph cantilever can be derived from Figure 2.5:

$$d = 2r\sin^2\left(\frac{\theta}{2}\right) = 2r\sin^2\left(\frac{L}{2r}\right) \tag{2.10}$$

where $\theta/2$ is defined as the deflection angle, and L is the length of the cantilever. For simplification, $L \approx L_0$, the small length change due to thermal expansion is neglected.

For small angles, $\sin\left(\frac{\theta}{2}\right) \approx \frac{\theta}{2} = \frac{L}{2r}$, thus Equations 2.9 and 2.10 combine to give:

$$d \approx \frac{L^2}{2r} = \frac{cxy(1+x)^2}{c^2x^4y^2 + 4cx^3y + 6cx^2y + 4cxy + 1} \cdot \frac{3\Delta\alpha \cdot \Delta T \cdot L^2}{t_1 + t_2} \tag{2.11}$$

Besides a mixed effect of relative width, thickness, and Young's modulus, the tip deflection varies linearly with $\Delta\alpha$, ΔT, and L^2, and is inversely proportional to the thickness. For the thermal bimorph cantilever of this study, $c = \frac{70/(1-0.35)}{169/(1-0.3)} = 0.4461$, $x = 2/5 = 0.4$, $y = 60/110 = 0.5455$, $\Delta\alpha = (23.1 - 2.6)\times10^{-6} = 2.05\times10^{-5}(K^{-1})$. Its deflection equation is: $d = 0.2484\Delta T(\mu m)$. Calculation and simulation data are plotted in Figure 2.6, showing good agreement.

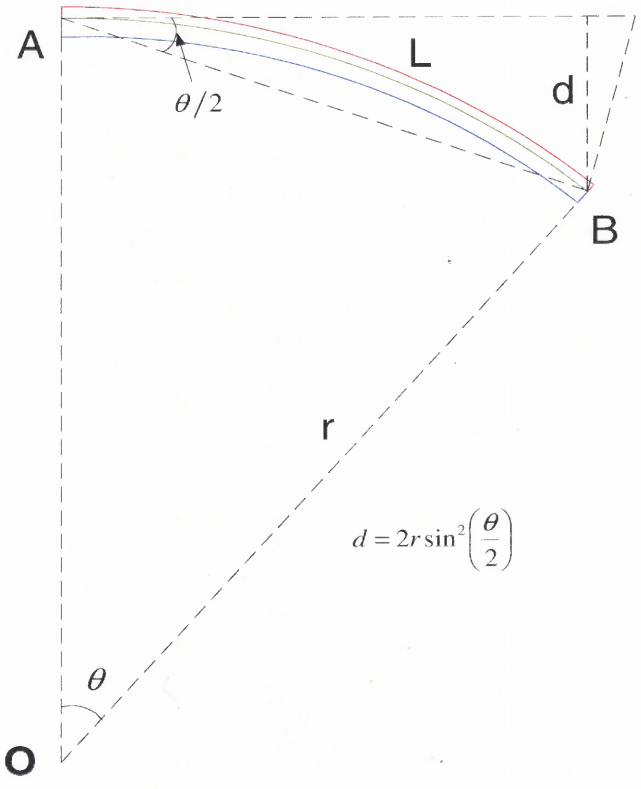

Figure 2.5 Schematic drawing of a bent bimorph cantilever.

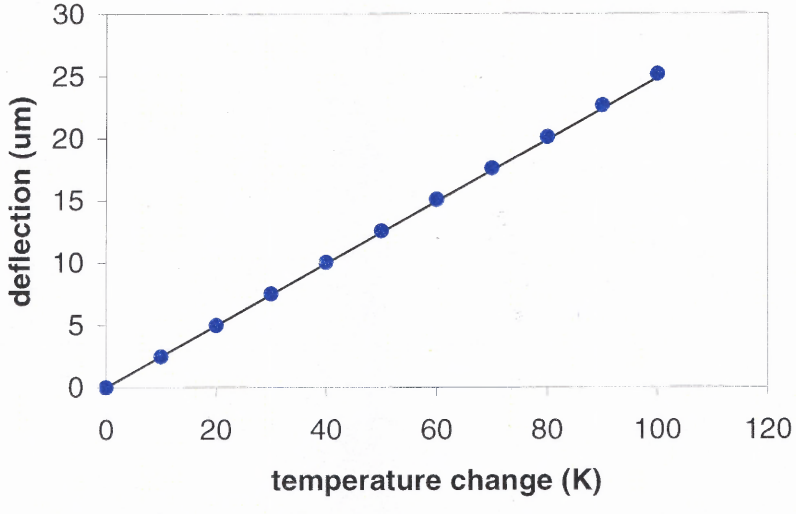

Figure 2.6 Calculated (line) and simulated (dot) tip deflection of the thermal bimorph cantilever of study.

When used as a sensor, a thermal bimorph cantilever needs to generate a large tip deflection for a given temperature change. According to Equation 2.11, it is clear that deflection is proportional to $\Delta\alpha$ and L^2, and inversely proportional to thickness. Therefore, thin and long beams with large TEC difference will have large deflection. The unknown effect is the mixed function of relative width, thickness, and Young's modulus, and the cantilever is optimized when this function has its maximum value. For optimization consideration, bimorph cantilevers are divided into two categories: either the total thickness is a constant or it contains one constant and one variable layer thickness.

2.2.1 Bimorph Cantilever with Constant Total Thickness

For a cantilever with constant total thickness, the deflection equation is:

$$d \approx \frac{cxy(1+x)^2}{c^2x^4y^2+4cx^3y+6cx^2y+4cxy+1} \cdot \frac{3\Delta\alpha \cdot \Delta T \cdot L^2}{t_1+t_2} \tag{2.12}$$

Since only the first part of the equation is subject to optimization, define:

$$f_1(x,y) = \frac{cxy(1+x)^2}{c^2x^4y^2+4cx^3y+6cx^2y+4cxy+1} \tag{2.13}$$

Function $f_1(x,y)$ is plotted in Figure 2.7, showing the existence of a maximum value. Taking the partial derivative of $f_1(x,y)$ with respect to x or y gives:

$$cx^2y = 1 \tag{2.14}$$

Putting Equation 2.14 back to 2.13, the maximum value of $f_1(x,y)$ is

$$f_{1(\max)} = 0.25 \tag{2.15}$$

And the deflection equation simplifies to:

$$d_{1(\max)} \approx \frac{3\Delta\alpha \cdot \Delta T \cdot L^2}{4(t_1 + t_2)} \tag{2.16}$$

This is an interesting and important result: it shows that the factor containing relative Young's modulus (c), thickness (x), and width (y) has a limit of 0.25, and the deflection of an optimized cantilever is independent of these parameters. A similar conclusion was made in [32] by a different approach. Equation 2.14 is called the optimum equation, which defines the relationships between c, x, and y to ensure a maximum deflection. For example, for an arbitrary material combination (different c) if the thickness of the second layer is selected, the corresponding width can be calculated from Equation 2.14 to optimize the cantilever deflection, and vice versa, as shown in Figure 2.8.

For this case, the TEC difference is the only material selection criterium. Of course, larger deflection is still possible for longer and thinner beams according to the deflection equation. Although Young's modulus does not change the maximum deflection, it is better to choose a large value for a robust structure.

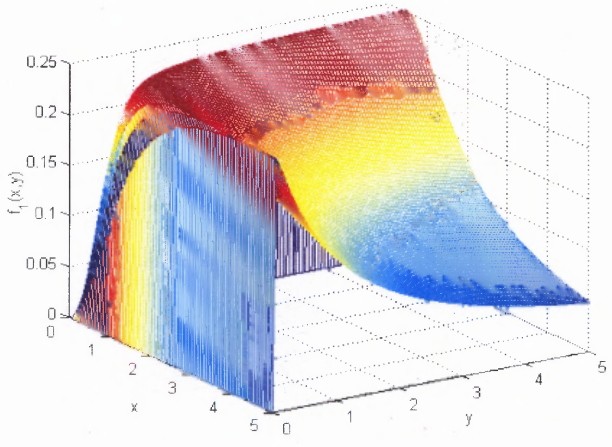

Figure 2.7 Function $f_1(x,y)$ for a given c.

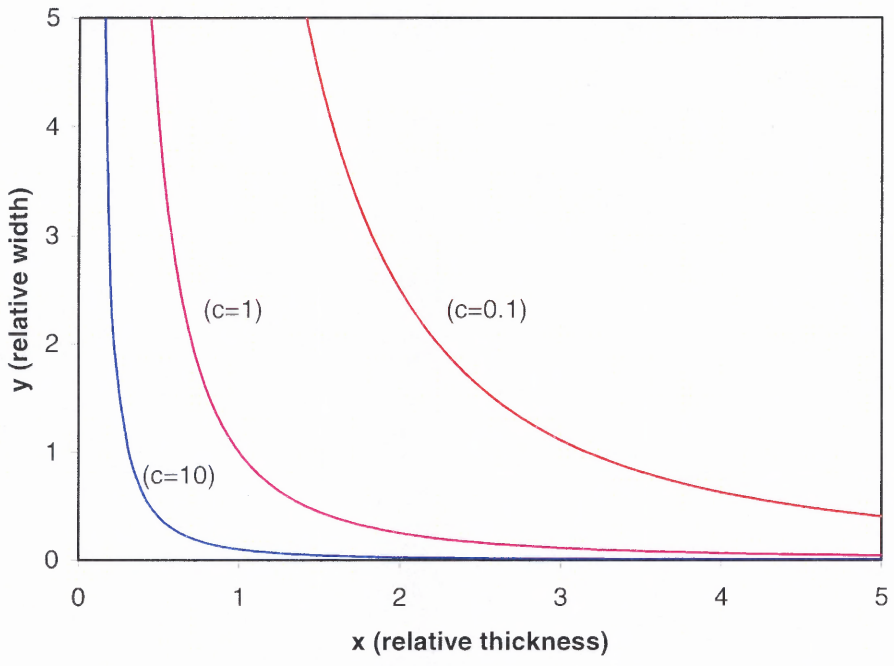

Figure 2.8 Optimum curves of Equation 2.14 for different relative Young's modulus values.

For the thermal bimorph cantilever of this study, if, for example, the width of the top aluminum layer changes from 10μm to 110μm, the corresponding layer thickness can be calculated from Equation 2.14 to ensure the maximum deflection (Equation 2.16). Since the total thickness is constant (7μm), the thickness of the silicon layer is determined. Calculation and simulation results are summarized in Table 2.2, showing good agreement. The tip deflection is 24.84μm and 54.91μm before and after optimization, respectively, for a temperature change of 100K.

Table 2.2 Calculated and simulated maximum deflections of the thermal bimorph of this study for different Al layer widths ($\Delta T = 100K$)

Al width (μm)	10	20	30	40	50	60	70	80	90	100	110
Al thickness (μm)	5.83	5.45	5.19	4.99	4.83	4.69	4.57	4.46	4.36	4.28	4.20
Si thickness (μm)	1.17	1.55	1.81	2.01	2.17	2.31	2.43	2.54	2.64	2.72	2.80
Simulated Deflection (μm)	54.7	54.9	55.1	55.6	55.8	56.2	56.7	57.1	57.6	58.1	58.5
Calculated Deflection (μm)	54.91										

2.2.2 Bimorph Cantilever with One Constant and One Variable Layer Thickness

In thin film technologies, the total thickness of fabricated bimorph cantilevers is not always constant. Most of the time only the substrate thickness is fixed, while the deposited layer is variable. Finding the optimum condition for this case is needed. Similar to the previous case, rearrange Equation 2.11 to:

$$d \approx \frac{cxy(1+x)}{c^2x^4y^2+4cx^3y+6cx^2y+4cxy+1} \cdot \frac{3\Delta\alpha \cdot \Delta T \cdot L^2}{t_1} \tag{2.17}$$

Since only the first part of the equation is subject for optimization, define:

$$f_2(x,y) = \frac{cxy(1+x)}{c^2x^4y^2+4cx^3y+6cx^2y+4cxy+1} \tag{2.18}$$

Taking the partial derivative of $f_2(x,y)$ with respect to x or y gives:

$$\frac{\partial f_2(x,y)}{\partial x} = 0$$
$$\Rightarrow 2x^3 + 3x^2 - \frac{1}{cy} = 0 \tag{2.19}$$

$$\frac{\partial f_2(x,y)}{\partial y} = 0$$
$$\Rightarrow cx^2y = 1 \tag{2.20}$$

Puting Equation 2.19 and 2.20 back to Equation 2.18 gives:

$$f_2(x)_{\max} = \frac{2x+3}{12(1+x)^2} \tag{2.21}$$

$$f_2(y)_{\max} = \frac{1}{4(1+1/\sqrt{cy})} \tag{2.22}$$

Unlike the previous case, here the optimum equations are different for the derivatives with respect to x and y. This means that the selection of the optimum equation is variable: if the relative width is constant, then Equation 2.19 should be used; if the relative thickness is constant, then Equation 2.20 should be used. Furthermore, the maximum value of function $f_2(x,y)$ is not a constant, as was the case in Figure 2.9. But from Equation 2.21 and 2.22, it can be derived that when $x \to 0$, $f_2(x)_{\max} \to 1/4$, and when $cy \to \infty$, $f_2(y)_{\max} \to 1/4$. So the limit is still valid, except this time it can only be approached but never be achieved.

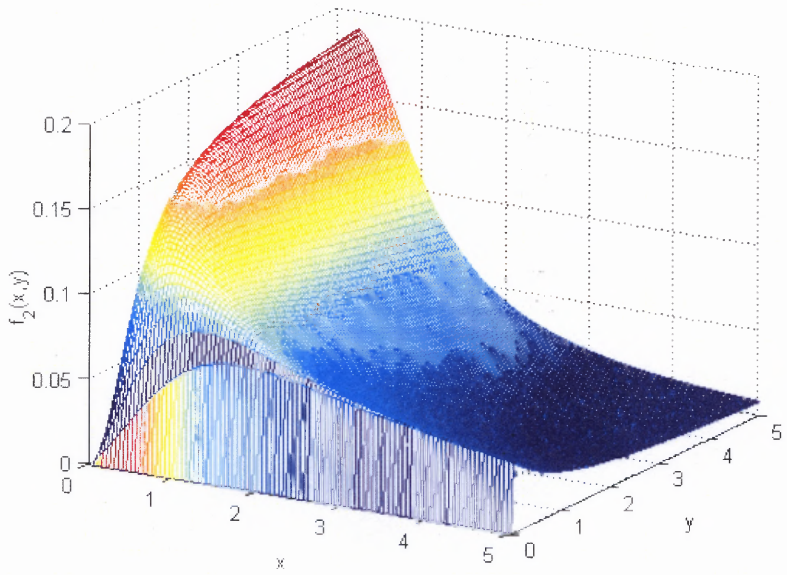

Figure 2.9 Function $f_2(x,y)$ for a given c.

Generally speaking, in order to approach for the limit, the second layer should be thin, wide, and hard compare to the substrate. Function $f_2(x,y)$ for $y = 1$ is plotted in Figure 2.10. It is clear that when c increases, the maximum value of $f_2(x,y)$ increases and the relative thickness decreases. The bold line represents the maximum values for different c. The material selection criteria for this case are given in the following steps:

Step 1: design the second layer as wide as possible ($y_{max}=1$),

Step 2: calculate x from Equation 2.19,

Step 3: calculate $f_2(x)_{max}$ from Equation 2.21,

Step 4: define $\Gamma = f_2(x)_{\max} \times \Delta\alpha$.

The best material combination is the one with the largest Γ, which is generally the one with the largest TEC difference, as in the previous case.

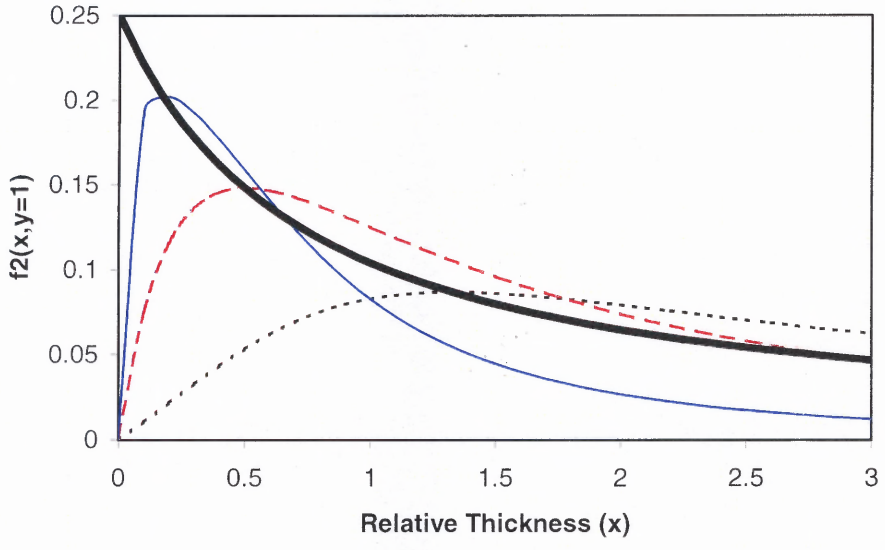

Figure 2.10 Function $f_2(x,y=1)$ for different value of relative Young's modulus: short dash ($c=0.1$), long dash ($c=1$), solid line ($c=10$). The bold line represents the maximum values. It goes down with the relative Young's modulus.

In real applications, the thickness of the second layer is always to be determined for optimization. Hence, the cubic Equation 2.19 needs to be solved. Since the constant in the equation is negative, there is one and only one positive root, as shown in Figure 2.11. This root is given by:

$$x=\sqrt[3]{\frac{1}{4cy}-\frac{1}{8}+\frac{\sqrt{1-cy}}{4cy}}+\sqrt[3]{\frac{1}{4cy}-\frac{1}{8}-\frac{\sqrt{1-cy}}{4cy}}-\frac{1}{2} \tag{2.23}$$

where c and y are relative Young's modulus and width, respectively.

Equation 2.23 is valid when $cy \leq 1$. For $cy > 1$, complex roots are obtained. This can be avoided by applying the exponential form of the complex number. Let $\frac{1}{4cy}-\frac{1}{8}=m$ and $\frac{\sqrt{cy-1}}{4cy}=n$. Thus Equation 2.23 can be transformed to:

$$\begin{aligned} x&=\sqrt[3]{m+ni}+\sqrt[3]{m-ni}-\frac{1}{2} \\ &=\sqrt[3]{\sqrt{m^2+n^2}\cdot e^{j\phi}}+\sqrt[3]{\sqrt{m^2+n^2}\cdot e^{-j\phi}}-\frac{1}{2} \\ &=\left(m^2+n^2\right)^{1/6}\cdot e^{j\phi/3}+\left(m^2+n^2\right)^{1/6}\cdot e^{-j\phi/3}-\frac{1}{2} \\ &=\left(m^2+n^2\right)^{1/6}\cdot\left(e^{j\phi/3}+e^{-j\phi/3}\right)-\frac{1}{2} \\ &=\cos\frac{\phi}{3}-\frac{1}{2} \end{aligned} \tag{2.24}$$

where $\phi=\tan^{-1}\frac{n}{m}=\tan^{-1}\left(\frac{2\sqrt{cy-1}}{2-cy}\right)$ and $\phi\in[0,\pi)$.

Note that the imaginary parts canceled out during the calculation, and Equation 2.24 provides a real positive value.

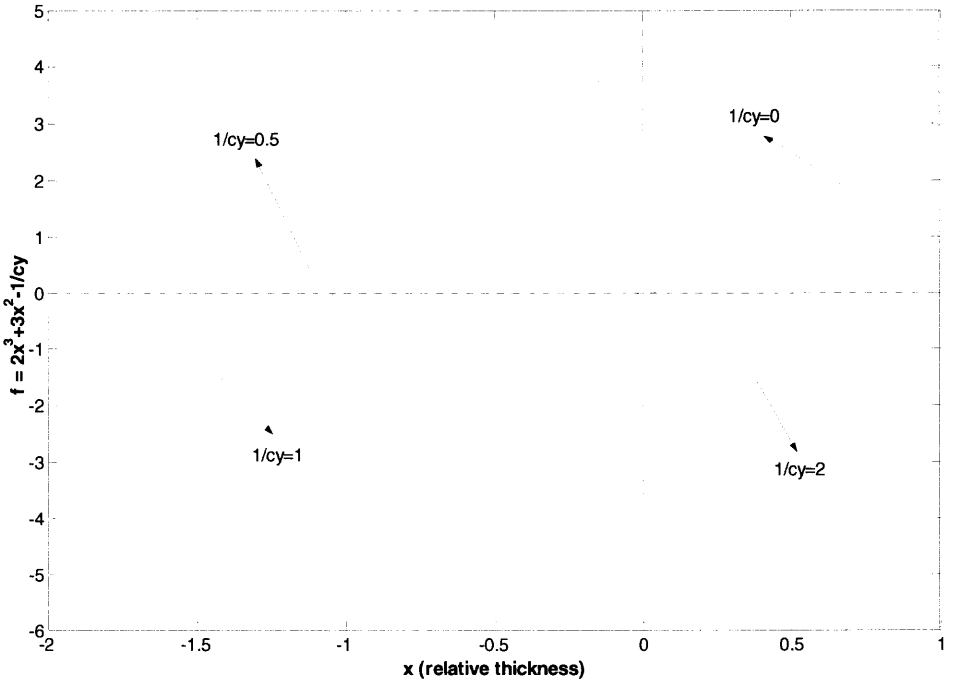

Figure 2.11 Curves of cubic Equation 2.19 with different negative constant terms, showing one and only one real positive root.

To demonstrate the use of the optimization procedure and equation, the bimorph cantilever of this study is optimized here: first, expand the line width of Al layer to 15μm, corresponding to a total width of 90μm. Since $y = 90/110 = 0.8182$, the relative thickness (x) is 0.7757 from Equation 2.23, corresponding to a real Al layer thickness of 3.88μm. The same result can be derived by calculation or simulation (Figure 2.12). The deflection goes up with the thickness of the Al layer to a maximum value (36.99μm), and then drops. For comparison, optimization is also performed for the cantilever without changing the width. This time, $y = 60/110 = 0.5455$ and $x=0.9212$, making the thickness of Al layer to be 4.61μm. The deflection is less than the first case (33.62μm).

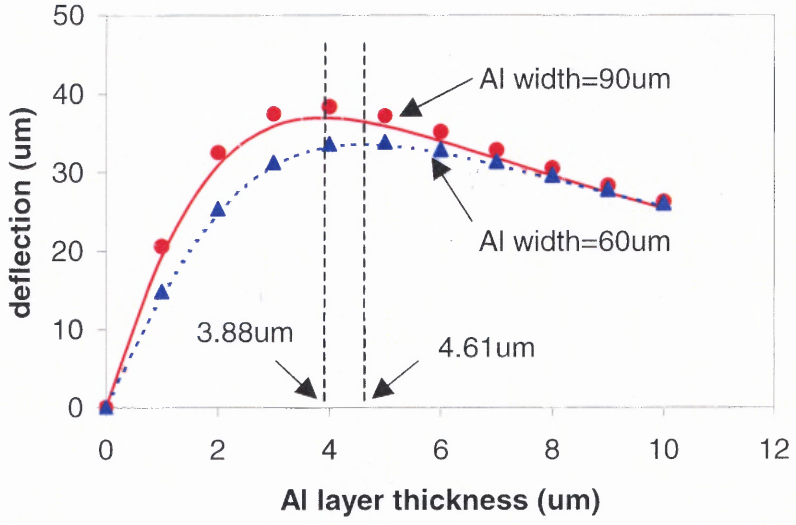

Figure 2.12 Calculated (lines) and simulated (dots) deflection for different Al layer widths. The wider layer (solid line and round dot) gives a larger deflection. The optimum Al layer thickness for each case is calculated directly from Equation 2.23 ($\Delta T = 100K$).

2.3 Static Temperature Distribution

Ideally, the bimorph cantilever should have low power consumption. To reach an optimal thermal efficiency, it is necessary to understand the different effects that can influence the optimum behavior of the bimorph cantilever. For this, the whole structure must be taken into consideration, which includes the device, the substrate and the surrounding air. Several effects, like the temperature distribution and thermal losses to the substrate and surrounding air are of great interest for optimization.

There are three heat transfer mechanisms: conduction, convection and radiation. Conduction occurs in a solid structure due to temperature gradient. It can be expressed as:

$$q_{conduction} = \lambda \cdot \frac{dT}{dx} \tag{2.25}$$

where λ is the thermal conductivity of material.

Convective heat transfer occurs between a fluid or air in motion and a bounding surface when the two are at different temperatures. Newton's law of cooling states:

$$q_{convection} = \alpha \cdot (T_{surface} - T_{ambient}) \tag{2.26}$$

where $q_{convection}$ is the convective heat flux (W/m^2) and is proportional to the difference between the surface and ambient temperatures. The value α is known as the convection heat transfer coefficient ($W/m^2 \cdot K$). Typical values are:

- Free convection gas: 2-25
- Free convection liquids: 50-1000
- Forced convection gas: 25-250
- Forced convection liquids: 50-20,000

Radiation heat transfer is the process by which thermal energy is exchanged between two surfaces obeying the laws of electromagnetics. The rate of heat flow by radiation is

$$q_{radiation} = \sigma_{S-B} \cdot \varepsilon \cdot (T^4{}_{surface} - T^4{}_{ambient}) \tag{2.27}$$

where σ_{S-B} is the Stefan-Boltzmann constant (5.67e-8 $W/K^4 \cdot m^2$) and ε is the emissivity of the surface which is between zero and 1 (blackbody).

An analytical model for the static temperature distribution in a cantilever has been developed [42]. The basic model considers a uniform internal heat source, and takes into account the conduction in the cantilever and convection to the surrounding gas. The radiation is neglected for simplification, since the maximum temperature of the cantilever is assumed to be less than 500K. The problem is stationary, corresponding to a DC drive of the cantilever. The temperature can be considered to be uniform throughout the cantilever thickness since it's very thin. So the heat transfer in the z-direction is reduced

to convection through the surface. Furthermore, the temperature throughout the cantilever width is considered to be uniform (y-direction). Thus, the problem can be simplified to a one-dimensional case, where the temperature is only a function of the position x along the cantilever length (Fig. 2.13).

In the steady state, the energy conservation law implies that for any unit cell of the cantilever, the heat generated inside the cell plus the heat flowing into the cell is equal to the heat that flows out plus the heat lost by convection on both surfaces:

$$Q_J + Q_{in} = Q_{out} + 2Q_{conv} \tag{2.28}$$

The terms in Equation 2.28 can be written as follows:

$$Q_J = q_j \cdot dx \cdot dy \tag{2.29}$$

$$Q_{in} = -\lambda \cdot \frac{dT(x)}{dx}\Big|_{x+dx} \cdot t \cdot dy \tag{2.30}$$

$$Q_{out} = -\lambda \cdot \frac{dT(x)}{dx}\Big|_{x-dx} \cdot t \cdot dy \tag{2.31}$$

$$Q_{conv} = \alpha \cdot [T(x) - T_{air}] \cdot dx \cdot dy \tag{2.32}$$

where, q_j is the electric power dissipated by Joule effect per unit surface, t is the cantilever thickness, λ is the thermal conductivity, and α is the convection heat transfer coefficient of the cantilever.

By inserting Equation 2.29 to 2.32 into Equation 2.28, it can be simplified to:

$$T''(x) - \frac{2\alpha}{\lambda \cdot t} T(x) = -\frac{q_j + 2\alpha T_{air}}{\lambda \cdot t} \tag{2.33}$$

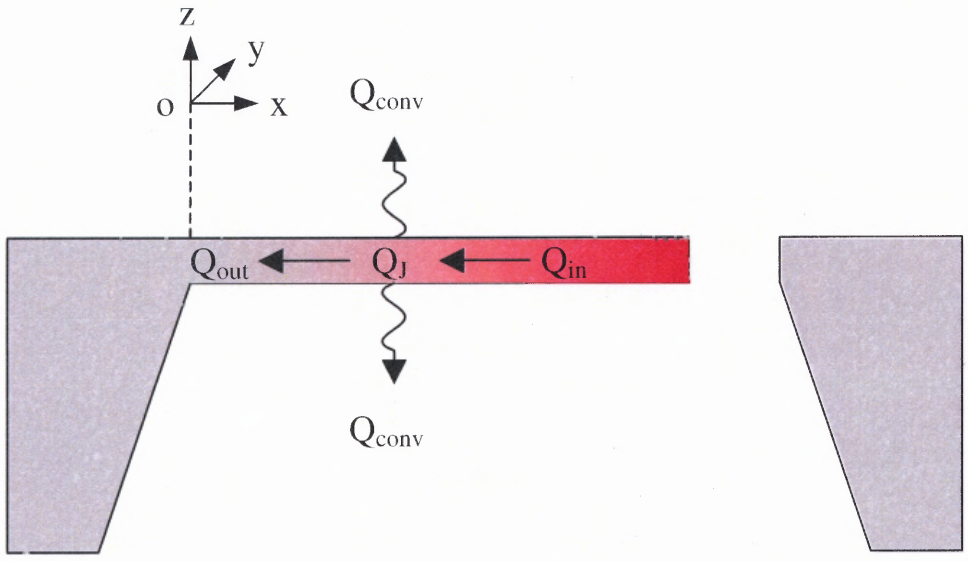

Figure 2.13 1D model of static temperature distribution in a thermal cantilever, consider a uniform internal heat source.

The solution form of the differential Equation 2.33 is [42, 20]:

$$T(x) = C_1 \cdot e^{\sqrt{\frac{2\alpha}{\lambda t}} \cdot x} + C_2 \cdot e^{-\sqrt{\frac{2\alpha}{\lambda t}} \cdot x} + C_3 \tag{2.34}$$

This is the static temperature distribution equation of the cantilever, where C_1, C_2, C_3 are constants, and can be determined by applying the following boundary conditions:

- By inserting Equation 2.34 into 2.33:

$$C_3 = T_{air} + \frac{q_j}{2\alpha} \tag{2.35}$$

- At $x=0$, the temperature in the cantilever is the same as in the substrate:

$$T(0) = C_1 + C_2 + C_3 = T_{sub} \tag{2.36}$$

- At $x=L$, at the end of the cantilever, heat transfer by conduction is zero,

$$\frac{d}{dx} T(x)\Big|_{x=L} = 0 \tag{2.37}$$

Assume $T_{sub} = T_{air}$, C_1 and C_2 can then be derived:

$$C_1 = -\frac{\frac{q_j}{2\alpha}\cdot e^{-\sqrt{\frac{2\alpha}{\lambda t}}\cdot L}}{e^{\sqrt{\frac{2\alpha}{\lambda t}}\cdot L}+e^{-\sqrt{\frac{2\alpha}{\lambda t}}\cdot L}} \tag{2.38}$$

$$C_2 = -\frac{\frac{q_j}{2\alpha}\cdot e^{\sqrt{\frac{2\alpha}{\lambda t}}\cdot L}}{e^{\sqrt{\frac{2\alpha}{\lambda t}}\cdot L}+e^{-\sqrt{\frac{2\alpha}{\lambda t}}\cdot L}} \tag{2.39}$$

Equation 2.34 can then be written as:

$$T(x) = \frac{q_j}{2\alpha}\cdot\left(1-\frac{\cosh\left(\sqrt{\frac{2\alpha}{\lambda t}}\cdot(L-x)\right)}{\cosh\left(\sqrt{\frac{2\alpha}{\lambda t}}\cdot L\right)}\right)+T_{air} \tag{2.40}$$

If convection is neglected, ($\alpha = 0$), Equation 2.33 is reduced to:

$$T''(x) = -\frac{q_j}{\lambda\cdot t} \tag{2.41}$$

Follow the same procedure as for Equation 2.40, the solution for Equation 2.41 is:

$$T(x) = -\frac{q_j}{2\lambda t}\cdot x^2 + \frac{q_j L}{\lambda t}\cdot x + T_{air} \tag{2.42}$$

The study above is done for a stationary state of the system, thus the temperature and device displacement are stable in time. It is considered that the cantilever is in a free convection state when driven in a DC mode. If the cantilever is actuated at the resonance frequency (AC mode) and the deflection oscillates, it is subjected to a forced convection. However, when the cantilever is resonating above the thermal cut-off frequency, the temperature variation over time is low. In this case, the cantilever is also considered to be in a stationary state.

For the thermal bimorph cantilever of this study, the resistance of the Al layer is about 3.98Ω. For a driving voltage of 0.5V, the corresponding input power is about 62.8mW. The mean thermal conductivity λ is determined by the contribution of each layer (164W/m-K). The temperature distribution can be calculated from Equation 2.40 or 2.42. Figure 2.14 is the simulated temperature distribution and deflection for the cantilever. The temperature increases with the length as expected, and is uniform in the width and thickness, which confirms the assumptions made earlier. The tip deflection is about 17.08μm with a maximum temperature of 439K (the environment temperature is 300K).

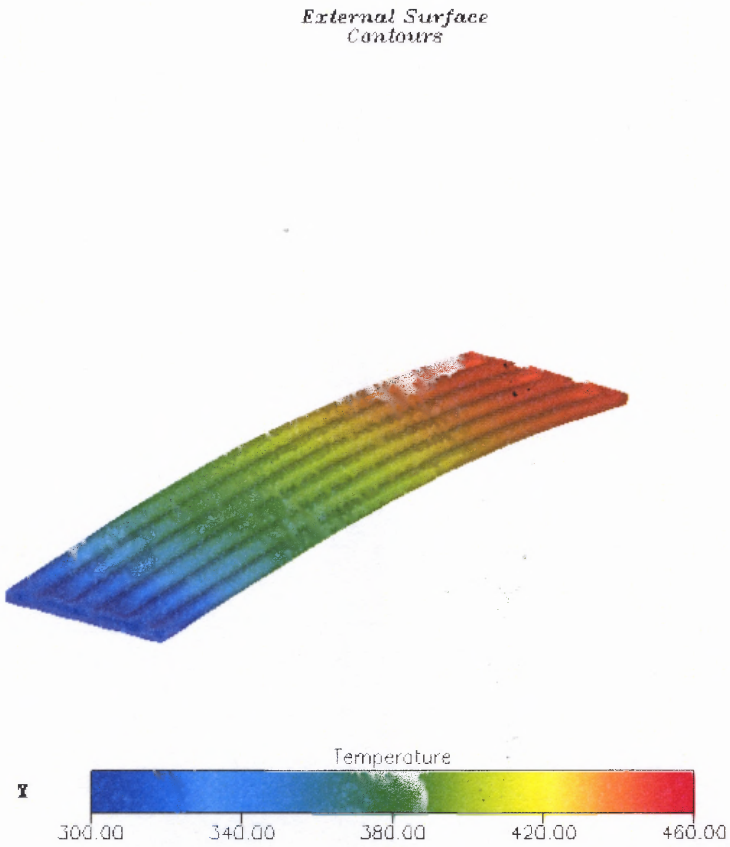

Figure 2.14 Temperature distribution and deflection of the thermal bimorph cantilever of study. Driving voltage is 0.5V.

2.3.1 Power and Deflection

From Equations 2.40 and 2.42, it is clear that the temperature of a position along the cantilever is linearly proportional to the heating power. Since deflection is proportional to temperature, it implies a linear relationship between power and deflection. Although the temperature distribution is not uniform, for any small segment along the length of the cantilever, the temperature distribution can be treated as uniform. Thus, the deflection equation is still valid within this area, and the total deflection is an integral along the whole cantilever length. Figure 2.15 is the simulated results of deflection and power for the thermal bimorph cantilever of this study. A good linear relationship is obtained.

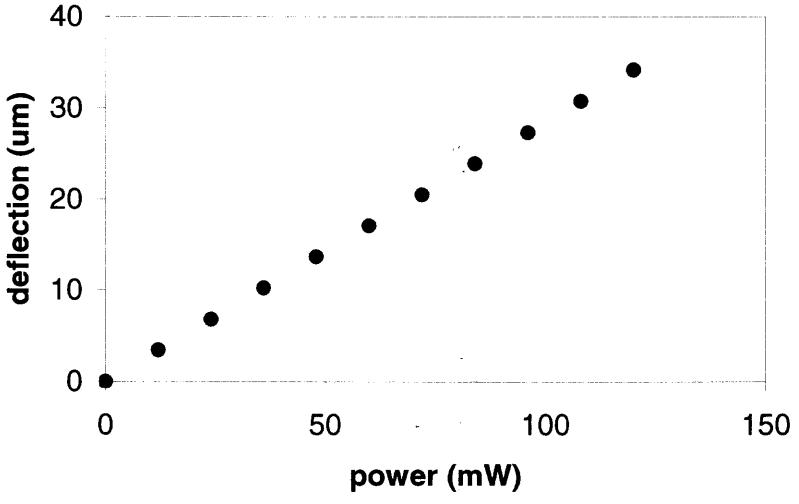

Figure 2.15 Linear relationship between power and deflection for the thermal bimorph cantilever of this study.

2.3.2 Effect of Convection

The typical value of heat transfer coefficient α is 2-25W/m^2 for free convection, and 25-250W/m^2 for forced convection. The effect of α on the temperature distribution of the thermal bimorph cantilever of this study is presented in Figure 2.16. Calculation data are from Equations 2.40 and 2.42. Since the Al layer is narrower than the silicon layer, its effective thickness is $\frac{60}{110}\times 2 = 1.09um$ for the temperature distribution calculation. It is clear that convection is not a dominant factor in this case for power dissipation. This is because only a small part of the heat is lost by convection to the air, and most of the generated heat is dissipated by conduction into the silicon substrate. As a matter of fact, the heat lost by conduction can be calculated by integrating Equation 2.31 over the contact area at *x=0*, which is 100% for $\alpha = 0(W/m^2 \cdot K)$, 99% for $\alpha = 25(W/m^2 \cdot K)$, and 95% for $\alpha = 250(W/m^2 \cdot K)$. The maximum temperature difference at the free end is 7.1K, and the deflection change is 0.6μm for a total of 17μm. The effect of radiation is even smaller for this temperature range. In fact, the simulation results both with and without considering radiation are almost the same.

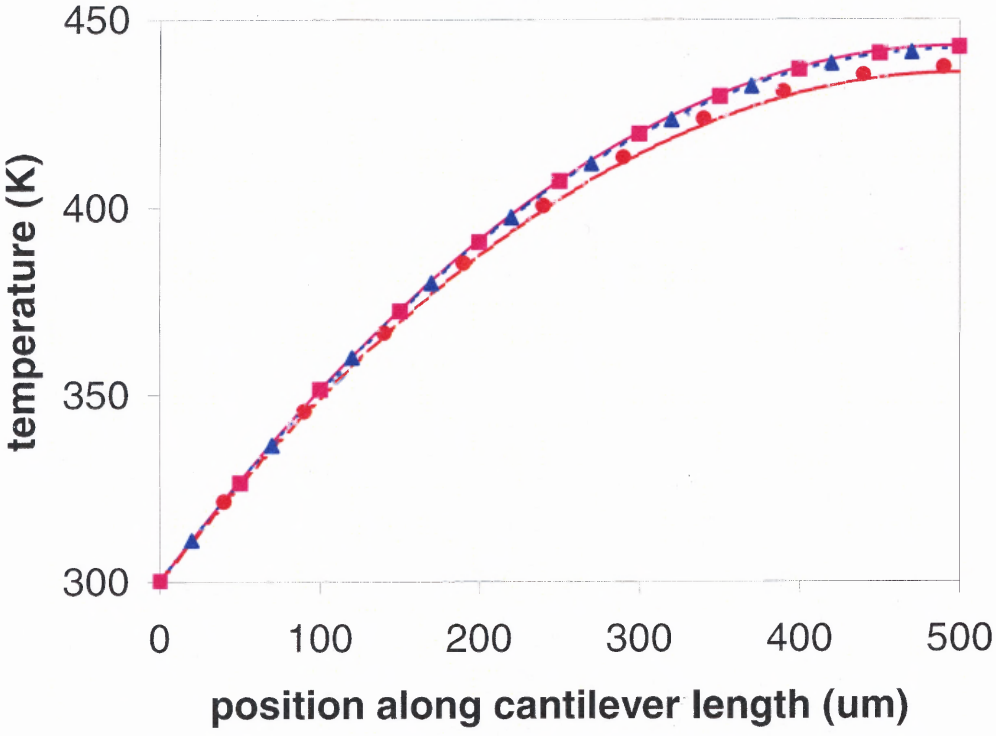

Figure 2.16 Calculated (lines) and simulated (dots) temperature distribution of the bimorph cantilever of this study for different heat transfer coefficients: $\alpha=0$ (solid line and square dot), $\alpha=25 W/m^2\text{-}K$ (short dash line and triangle dot), and $\alpha=250 W/m^2\text{-}K$ (long dash line and round dot). Note the small differences.

2.3.3 Effect of Thermal Conductivity

The influence of heat conduction in the beam is very important. According to Equation 2.40 and 2.42, decreasing λ increases the temperature, since heat is less likely to be transferred through the substrate. Therefore, less power is needed to achieve a certain temperature. In order to reduce the power consumption, materials with low thermal conductivity, such as SiO_2, should be used.

2.3.4 Effect of Dimension

Generally, a cantilever with less contact area with the substrate is less favorable for conducting heat. Therefore, the power consumption is less for thin and narrow beams. Moreover, when the beam length increases, the average temperature of the cantilever also increases for a given power, which implies less power loss. Indeed, this has been reported experimentally: shorter beams show higher power consumption than longer beams. Of course, the beam length cannot be increased indefinitely due to considerations such as sensitivity to vibrations, shocks, as well as mechanical resonance behavior. A compromise has to be found between thermal efficiency and mechanical stability.

2.4 Dynamic Behavior

The effective response time of the thermal bimorph cantilever is of great interest in applications, especially for a resonant driving mode. The thermal time constant (τ) of a cantilever is the characteristic time it takes for the cantilever to come to rest at a new position after a sudden change of the supply power. For a given heating period, the time constant is defined in:

$$d = d_0(1-e^{-t/\tau}) \tag{2.43}$$

And for a given cooling period, it defined in:

$$d = d_0 e^{-t/\tau} \tag{2.44}$$

where d is the deflection after change, d_0 is the original deflection, and t is the time.

The transitory behavior of the thermal bimorph cantilever of this study during heating and cooling periods is plotted in Figure 2.17. From the fitting curve, it is easy to extract the thermal time constant, which is about 1.1ms.

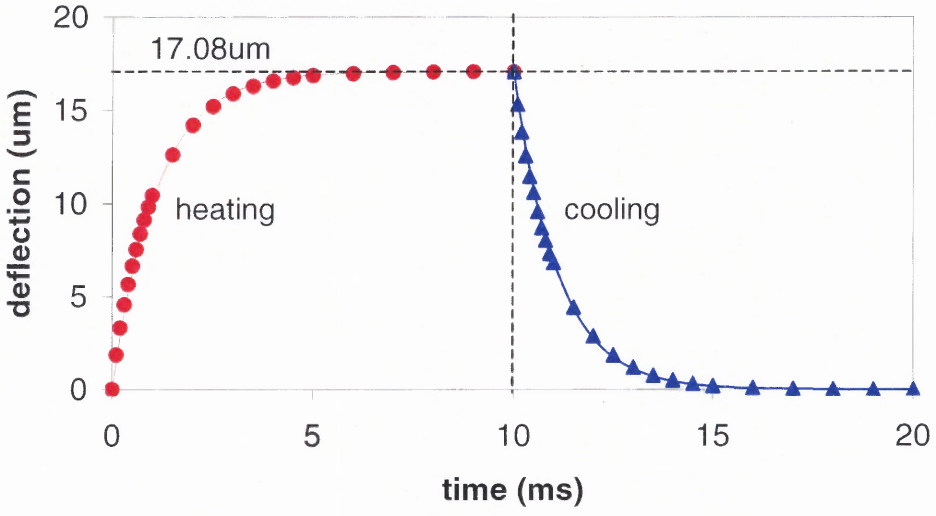

Figure 2.17 Transitory behavior and fitting curves of the thermal bimorph cantilever of this study during heating and cooling. The limit (17.08μm) is the static deflection for the given power (62.8mW).

For a simple 1-D model, the time constant of the cantilever is derived [42]:

$$\tau = \frac{\rho \cdot c \cdot L^2}{2\lambda} \tag{2.45}$$

where ρ is the mean mass density, c is the mean specific heat capacity, λ is mean thermal conductivity, and L is the length.

This implies that in order to have a fast response time, materials with less density, less heat capacity, and large thermal conductivity should be chosen. Also the beam should be short, in conflict with the low power consumption requirement for a longer beam. For the bimorph cantilever of this study, the calculated time constant is about 1.36ms, comparde to the value derived from Figure 2.17 (1.1ms).

When the cantilever is driven in th AC mode, the average power is half the maximum power for a square wave, and the average deflection of the cantilever is half

the maximum value since deflection is proportional to power. The cantilever can be treated as being equivalent to vibrating around the half power deflection position, with the maximum of full power deflection and the minimum of zero. When the frequency increases, there is not enough time for the cantilever to achieve the maximum and minimum values. Therefore, its vibrating amplitude decreases. Figure 2.18 demonstrates this phenomenon: when the frequency is low, there is enough time for the cantilever to achieve both the upper (17.08μm) and lower (zero) limits. Its vibrating amplitude is 17.08μm (as in Figure 2.17). When the frequency increases to 125Hz, the vibration amplitude drops to 15.93μm. When the frequency increases to 250Hz, the amplitude is 12μm. If the frequency is high enough, the amplitude will drop to zero and the cantilever will stop at the half power position (8.54μm).

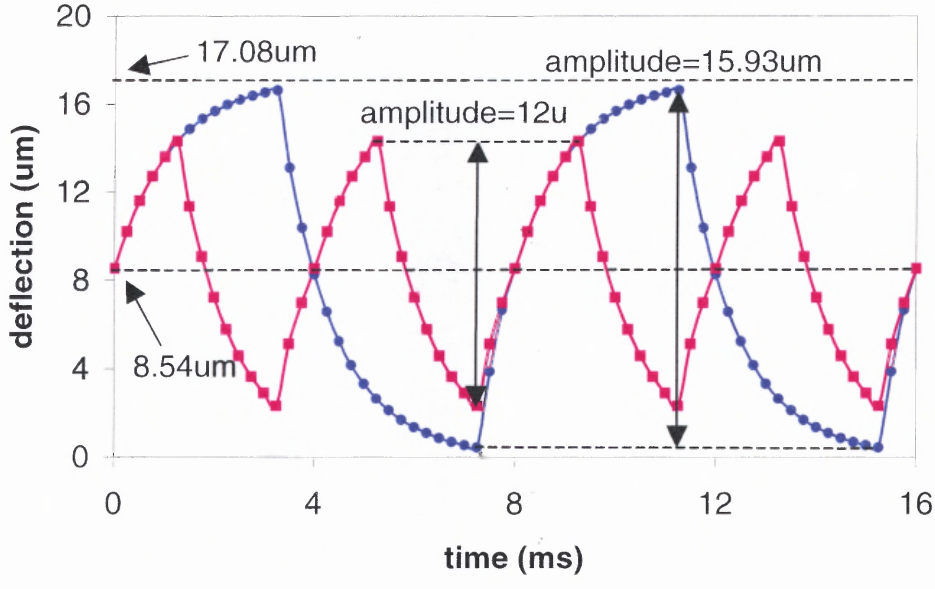

Figure 2.18 The dependence of vibrating amplitude on frequency of the thermal bimorph cantilever for this study.

Since the amplitude of the cantilever is frequency dependent, a cut-off frequency is introduced, which is defined as the frequency at which the vibrating amplitude drops to a certain portion of the low frequency value. Based on the symmetry of the heating and cooling period, the cut-off frequency can be derived:

$$f_{cut-off} = \frac{1}{2\tau \ln\left(\frac{1+p}{1-p}\right)} \tag{2.46}$$

where τ is the time constant and p is the ratio between the set point and static value.

Since the cut-off frequency is inversely proportional to τ, all the factors that are good for giving a short time constant are also good for achieving a higher cut-off frequency. For the cantilever of this study, its –3dB cut-off frequency is calculated as 208Hz (τ=1.36ms) and 257Hz (τ=1.1ms), compared to the cut-off frequency derived from Figure 2.19 (250Hz).

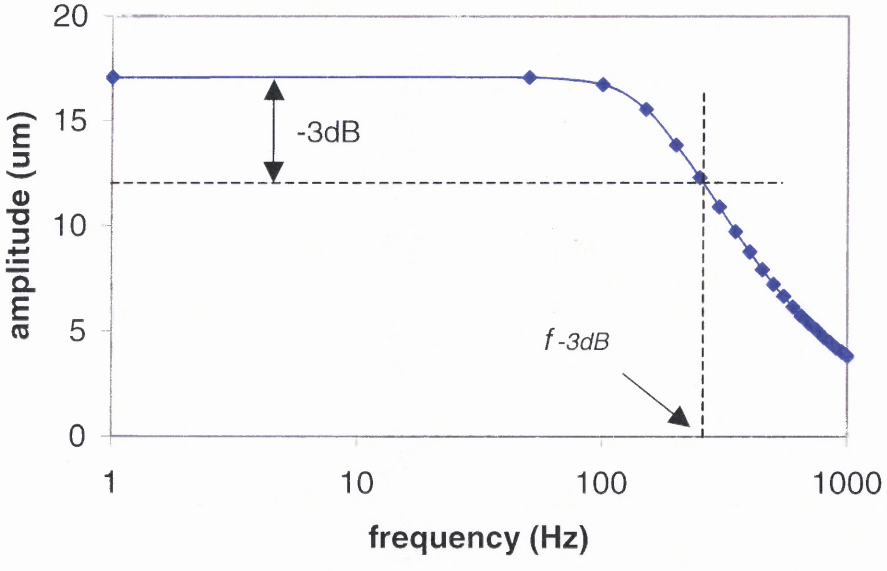

Figure 2.19 Simulated frequency response of the cantilever of this study.

2.5 Summary

The purpose of this chapter was to study and understand the thermal bimorph cantilever for better understanding of the relations between performance and design parameters. Optimizations for deflection are performed for bimorph cantilevers with a) a constant total thickness or b) one constant and one variable layer thickness. Optimum equations are then derived for each case. A good agreement is found between calculation and simulation results. Technological constraints must also be considered. It is found that in the free convection mode, the losses by convection are not dominant. The largest part of the generated heat is lost by conduction in the silicon. The thermal time constant calculation gives the design rules that the thermal cut-off frequency goes down with the square of the beam length. Faster response time requires high thermal diffusivity constants, thus high thermal conductivities and short beams. This is in contrast with the requirements for a low power consumption beam. Depending on the application, a compromise has to be found between low power consumption and short response time. For a given applied power on the beam, the average temperature increases as the beam length increases and the beam thickness decreases. A compromise was found between thermal efficiency and mechanical stability.

CHAPTER 3

ELECTROSTATIC TORSION ACTUATORS

3.1 Round Electrostatic Torsion Actuator

3.1.1 Theoretical Study

Figure 3.1 presents a schematic view of the round, double-gimbaled system, showing the various relevant parameters. The inner round plate is made to rotate about the y-axis by electrostatic actuation using either electrode E_{in1} or E_{in2} under the round plate. The outer ring rotates the full structure about the x-axis by electrostatic actuation using either electrode E_{out1} or E_{out2} under the outer ring. The two inner springs along the y-axis connect the inner round plate to the outer ring. The two outer springs along the x-axis connect the outer ring to the fixed ring. The radius of the inner round plate is r. The inner and outer radii of the outer ring are r_1 and r_2, respectively. The distance from the center of the inner springs to the end of electrode E_{in1} or E_{in2} is a. The distance from the center of the outer springs to the end of electrode E_{out1} or E_{out2} is b. The structure thickness is w. The air gap depth is d. The length, height and thickness of each inner spring are l_{in}, h, and t_{in}, respectively. The length, height and thickness of each outer spring are l_{out}, h, and t_{out}, respectively. In this study, the spring height h equals the structure thickness w. The angle between the inner round plate and the fixed electrode plane is defined as α_{in} by electrostatic actuation using electrode E_{in1} in the A-A' view. The angle between the outer ring and the fixed electrode plane is defined as α_{out} by electrostatic actuation using electrode E_{out1}.

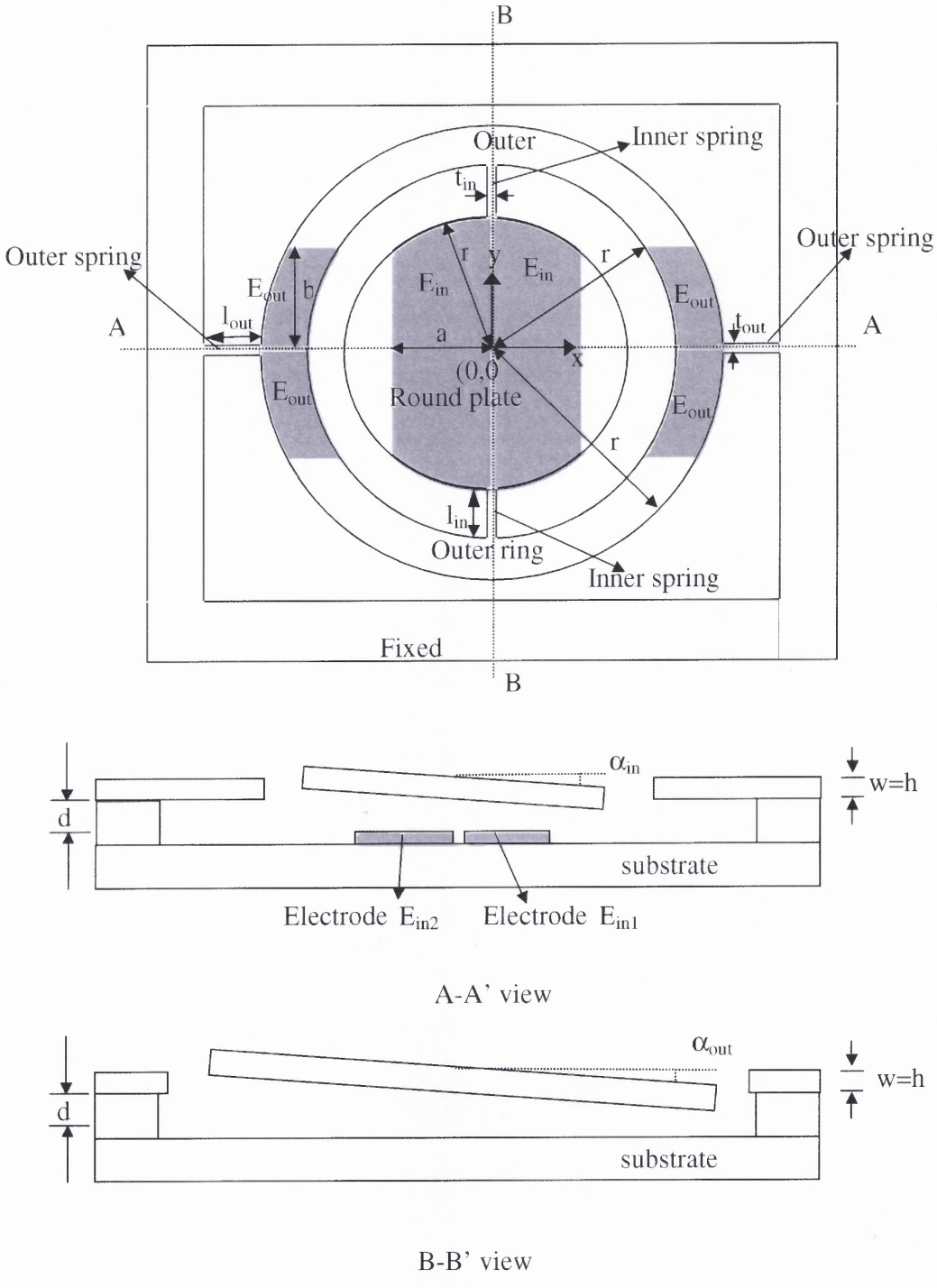

Figure 3.1 A schematic view of the round, double-gimbaled system, showing the various relevant parameters.

The inner round plate rotates about the y-axis by electrostatic actuation using buried electrodes E_{in1} or E_{in2}. The outer ring rotates the full structure about the x-axis by electrostatic actuation using buried electrodes E_{out1} or E_{out2}. The two inner springs along the y-axis connect the inner round plate to the outer ring. The two outer springs along the x-axis connect the outer ring to the fixed ring. The radius of the inner round plate is r. The inner and outer radii of the outer ring are r_1 and r_2, respectively. The distance from the center of the inner springs to the end of electrode E_{in1} or E_{in2} is a. The distance from the center of the outer springs to the end of either electrode E_{out1} or E_{out2} is b. The structure thickness is w. The length, height and thickness of each inner spring are l_{in}, h, and t_{in}, respectively. The length, height and thickness of each outer spring are l_{out}, h, and t_{out}, respectively. In this paper, the spring height equals w. The angle between the inner round plate and the fixed electrode plane is α_{in}. The angle between the outer ring and the fixed electrode plane is α_{out}.

For the inner round plate, if the applied voltage between the movable structure and the electrode E_{in1} is V_{in}, the electrostatic torque, M_e can be written as

$$M_e(\alpha_{in}) = \int_{a_1}^{a} \int_{-\sqrt{r^2-x^2}}^{\sqrt{r^2-x^2}} x P_e \, dy dx \tag{3.1}$$

where a_1 is the horizontal distance from the center of the inner springs to the nearest edge of the electrode E_{in1}. a_1 is generally much smaller than a and r and can be approximately treated as 0. P_e is the electrostatic pressure, which can be written as

$$P_e = \frac{\varepsilon_0 V_{in}^{\ 2}}{2(d-\Delta d)^2} \tag{3.2}$$

where Δd is the displacement by the electrostatic force at an arbitrary point on the round plate and ε_0 is the dielectric constant of the vacuum. At a small tilt angle α_{in}, Δd can be written as

$$\Delta d = x\tan(\alpha_{in}) \approx x\alpha_{in} \tag{3.3}$$

Substituting Equations 3.2 and 3.3 into Equation 3.1, yields

$$M_e(\alpha_{in}) = \int_0^a \int_{-\sqrt{r^2-x^2}}^{\sqrt{r^2-x^2}} \frac{x\varepsilon_0 V_{in}^{\ 2}}{2(d-x\alpha_{in})^2} dydx = \int_0^a \frac{x\sqrt{r^2-x^2}\,\varepsilon_0 V_{in}^{\ 2}}{(d-x\alpha_{in})^2} dx \tag{3.4}$$

Before pull-in, the mechanical torque, M_m equals the electrostatic torque M_e,

$$M_e(\alpha_{in}) = \int_0^a \frac{x\sqrt{r^2-x^2}\,\varepsilon_0 V_{in}^{\ 2}}{(d-x\alpha_{in})^2} dx = K_{\alpha in}\alpha_{in} + K_{3in}\alpha_{in}^{\ 3} = M_m(\alpha_{in}) \tag{3.5}$$

where $K_{\alpha in}$ is the linear mechanical spring constant of the inner spring. K_{3in} is the nonlinear mechanical spring constant. At small tilt angles, the contribution from the nonlinear mechanical torque can be neglected. In addition, the theory and equations used here have not considered the effects of either fringe fields or bending mode motion.

At the pull-in point, the mechanical spring constant K_α (i.e., $dM_m/d\alpha_{in}$) is equal to the electrostatic spring constant (i.e., $dM_e/d\alpha_{in}$). Thus differentiating Equation 3.5 with respect to α_{in}, multiplying by α_{in} and subtracting Equation 3.5, yields

$$\int_0^a \frac{x\sqrt{r^2-x^2}\,(d-3x\alpha_{pi})}{(d-x\alpha_{pi})^3} dx = 0 \tag{3.6}$$

where α_{pi} is the pull-in angle for the inner round plate.

Normalizing Equation 3.6 using $x=x'r$, $\alpha_{pi}=\theta_{pi}\alpha_{im}$ and $a=\beta_i r$, yields

$$\int_0^{\beta_i} \frac{x'\sqrt{1-x'^2}\,(1-3x'\theta_{pi})}{(1-x'\theta_{pi})^3} dx' = 0 \tag{3.7}$$

where α_{im} is the maximum tilt angle and approximately equals d/r. β_i is the ratio of the length of the buried electrode to the radius of the round plate.

The above equation defines the fractional tilt of the inner round plate at pull-in, θ_{pi}. θ_{pi} only depends on β_i. However, Equation 3.7 cannot be reduced to a simple expression, it can only be solved by analytical iteration.

Substituting θ_{pi} into Equation 3.5, the pull-in voltage V_{pi} for the inner round plate can be written as

$$V_{pi} = \left(\frac{K_{\alpha in}\theta_{pi} d^3}{r^4 \varepsilon_0} \frac{1}{\int_0^{\beta_i} \frac{x'\sqrt{1-x'^2}}{(1-x'\theta_{pi})^2} dx'} \right)^{1/2} \tag{3.8}$$

The linear spring constant can be calculated by using

$$K_{\alpha in} = \frac{Ght_{in}^3}{8l_{in}} \left[\frac{16}{3} - 3.36\frac{t_{in}}{h}\left(1 - \frac{t_{in}^3}{12h^3}\right) \right] \tag{3.9}$$

where G is the shear modulus and equals 0.73×10^{11}Pa for silicon [75].

Additional design generalizations can be made by normalizing the applied voltage and resulting tilt angle by their respective pull-in values in Equations 3.5 and 3.8. Thus taking $X_{in}=\alpha_{in}/\alpha_{pi}$ and $Y_{in}=V_{in}/V_{pi}$, the equations become

$$\frac{\int_0^{\beta_i} \frac{x'\sqrt{1-x'^2}}{(1-x'\theta_{pi}X_{in})^2} dx'}{\int_0^{\beta_i} \frac{x'\sqrt{1-x'^2}}{(1-x'\theta_{pi})^2} dx'} Y_{in}^{\ 2} = X_{in} \tag{3.10}$$

Equation 3.10 is a general structural equation for electrostatic torsion actuators with round plates. It predicts the displacement or tilt of the round actuator as a function of

applied voltage. The equation shows that the relationship between the normalized applied voltage and the normalized tilt angle only depends on the electrode length ratio β_i.

For the outer round ring, if the distance from the center of the outer springs to the nearest edge of the electrode E_{out1} or E_{out2} is much smaller than b, r_1 and r_2, then the electrostatic torque equals the mechanical torque, and can be written as

$$M_e(\alpha_{out}) = \int_0^b \int_{-\sqrt{r_2^2-y^2}}^{\sqrt{r_2^2-y^2}} \frac{y\varepsilon_0 V_{out}^2}{2(d-y\alpha_{out})^2} dxdy - \int_0^b \int_{-\sqrt{r_1^2-y^2}}^{\sqrt{r_1^2-y^2}} \frac{y\varepsilon_0 V_{out}^2}{2(d-y\alpha_{out})^2} dxdy = K_{\alpha out}\alpha_{out} + K_{3out}\alpha_{out}^3 \tag{3.11}$$

where $K_{\alpha out}$ is the spring constant of the outer springs. V_{out} is the applied voltage between the outer electrodes E_{out1} or E_{out2} and the movable plate. K_{3out} is the nonlinear mechanical spring constant. At small tilt angles, the contribution from the nonlinear mechanical torque can be neglected.

With the same approach used for the inner round plate, the pull-in angle α_{po} can be written as

$$\int_0^b \frac{y\sqrt{r_2^2 - y^2}(d - 3y\alpha_{po})}{(d - y\alpha_{po})^3} dy - \int_0^b \frac{y\sqrt{r_1^2 - y^2}(d - 3y\alpha_{po})}{(d - y\alpha_{po})^3} dy = 0 \tag{3.12}$$

and Equation 3.10 can be normalized as

$$\int_0^{\beta_o} \frac{y'\sqrt{1-y'^2}(1-3y'\theta_{po})}{(1-y'\theta_{po})^3} dy' - \int_0^{\begin{cases}\gamma(b\geq r_1)\\ or\\ \beta_o(b<r_1)\end{cases}} \frac{y'\sqrt{\gamma^2-y'^2}(1-3y'\theta_{po})}{(1-y'\theta_{po})^3} dy' = 0 \tag{3.13}$$

where β_o is the outer electrode length ratio and equals b/r_2, θ_{po} is the fractional tilt and equals α_{po}/α_{om}, α_{om} is the maximum tilt angle and approximately equals d/r_2, $\gamma=r_1/r_2$ and $y'=y/r_2$. Thus, the outer ring fractional tilt at pull in, θ_{po} is only dependent on γ and β_{po}.

Substituting θ_{po} into Equation 3.11, the pull-in voltage V_{po} for the outer round ring can be written as

$$V_{po} = \left(K_{\alpha out}\theta_{po} \times \frac{d^3}{\varepsilon_0 r_2^4} \left(\int_0^{\beta_o} \frac{y'\sqrt{1-y'^2}}{(1-y'\theta_{po})^2}dy' - \int_0^{\substack{\gamma(b\geq r_1) \\ or \\ \beta_o(b<r_1)}} \frac{y'\sqrt{\gamma^2-y'^2}}{(1-y'\theta_{po})^2}dy' \right) \right)^{1/2} \tag{3.14}$$

Additional design generalizations can also be made by normalizing the applied voltage and resulting tilt angle by their respective pull-in values in Equation 3.11 and 3.14. Thus taking $X_{out}=\alpha/\alpha_{po}$ and $Y_{out}=V_{out}/V_{po}$, the equations become

$$\frac{\int_0^{\beta_o} \frac{y'\sqrt{1-y'^2}}{(1-y'X_{out}\theta_{po})^2}dy' - \int_0^{\substack{\gamma(b\geq r_1) \\ or \\ \beta_o(b<r_1)}} \frac{y'\sqrt{\gamma^2-y'^2}}{(1-y'X_{out}\theta_{po})^2}dy'}{\int_0^{\beta_o} \frac{y'\sqrt{1-y'^2}}{(1-y'\theta_{po})^2}dy' - \int_0^{\substack{\gamma(b\geq r_1) \\ or \\ \beta_o(b<r_1)}} \frac{y'\sqrt{\gamma^2-y'^2}}{(1-y'\theta_{po})^2}dy'} Y_{out}^{\ 2} = X_{out} \tag{3.15}$$

Equation 3.15 is a general structural equation for electrostatic torsion actuators with ring plates. It predicts the displacement or tilt of the ring actuator as a function of applied voltage. The equation shows that the relationship between the normalized applied voltage and the normalized tilt angle only depends on the electrode length ratios β_o and γ.

3.1.2 Verification

To test the validity of the analytical expressions, comparisons are made between the analytical predictions and the results of MEMCAD 4.8 finite element simulation for a typical round, double-gimbaled device.

Table 3.1 compares the fractional tilts at pull-in and the pull-in voltages for the inner round plate at electrode length ratio β_i=0.44, 0.6, 0.8 and 1.0, using both MEMCAD simulations and the theoretical predictions of Equation 3.7 and 3.8. The actuator dimensions are r=200μm, l_{in}=100μm, h=w=10μm, t_{in}=3μm and d=7μm. For full plate electrodes (β_i=1), it is found that the maximum travel range before pull-in is about 48% deflection, while full travel without pull-in is obtained for electrode length ratios $\beta_i \leq 0.44$. As shown in the table, the factional differences between the MEMCAD simulations and the theoretical predictions are smaller than 4% both for the fractional tilts at pull-in and the pull-in voltages.

Table 3.2 compares the fractional tilts at pull-in and the pull-in voltages for the outer ring plate at electrode length ratio β_o=0.44, 0.6, 0.8 and 1.0, using both MEMCAD simulations and the theoretical predictions of Equation 3.13 and 3.14. The actuator dimensions are r_1=300μm, r_2=500μm, l_{out}=100μm, h=w=10μm, t_{out}=3μm and d=7μm. For full plate electrodes (β_i=1), it is found that the maximum travel range before pull-in is about 45% deflection, while full travel without pull-in is obtained for electrode length ratios $\beta_i \leq 0.44$. As shown in the table, the fractional differences between the MEMCAD simulations and the theoretical predictions are again smaller than 4% both for the fractional tilts at pull-in and the pull-in voltages. It can be concluded that the straightforward analytical approach provides a reasonable approximation to the more complex and time-consuming finite element analysis simulation method.

In tables 3.1 and 3.2, the product of electrode length ratio and fractional tilt at pull-in is also given. It is found that the value of this product ranges from 0.43 to 0.48 for the inner round ring, while for the outer ring, the product ranges from 0.41 to 0.46. It

should be noted that in both cases, the value of this product is close to 0.44, the value for rectangular actuators [74]. The fractional tilts at pull-in are approximately equal to 1 (i.e., full actuator travel range) for both the inner round plate and the outer ring when electrode length ratios are equal to 0.44. Finally, for completeness, the MEMCAD meshing element, node number and the convergence parameters are listed in the tables.

As a further demonstration of the validity of the analytical approach compare the predictions of Equation 3.10 and 3.15 to simulation results for actuator displacement as a function of applied voltage. Consider the same actuator design used in Tables 3.1 and 3.2.

Figures 3.2 and 3.3 show curves of X versus Y, the normalized applied voltage versus the normalized tilt angle, for the inner round and outer ring plates, respectively. Data is presented for values of at β=0.44, 0.6, 0.8 and 1.0. The analytical predictions are in good agreement with the MEMCAD simulation results.

Finally, compare the results of Equation 3.10 for round plates with previously published results for rectangular plates. Equation 3.16 gives the general structural equation for electrostatic torsion actuators with rectangular plates [74].

$$\frac{Y^2}{X^3}\frac{\left[\dfrac{1}{1-0.44X}-1+\ln(1-0.44X)\right]}{0.2065}\cong 1 \tag{3.16}$$

Figure 3.2 shows that the curve of X versus Y for actuators with rectangular plates is nearly indistinguishable from that for round plates.

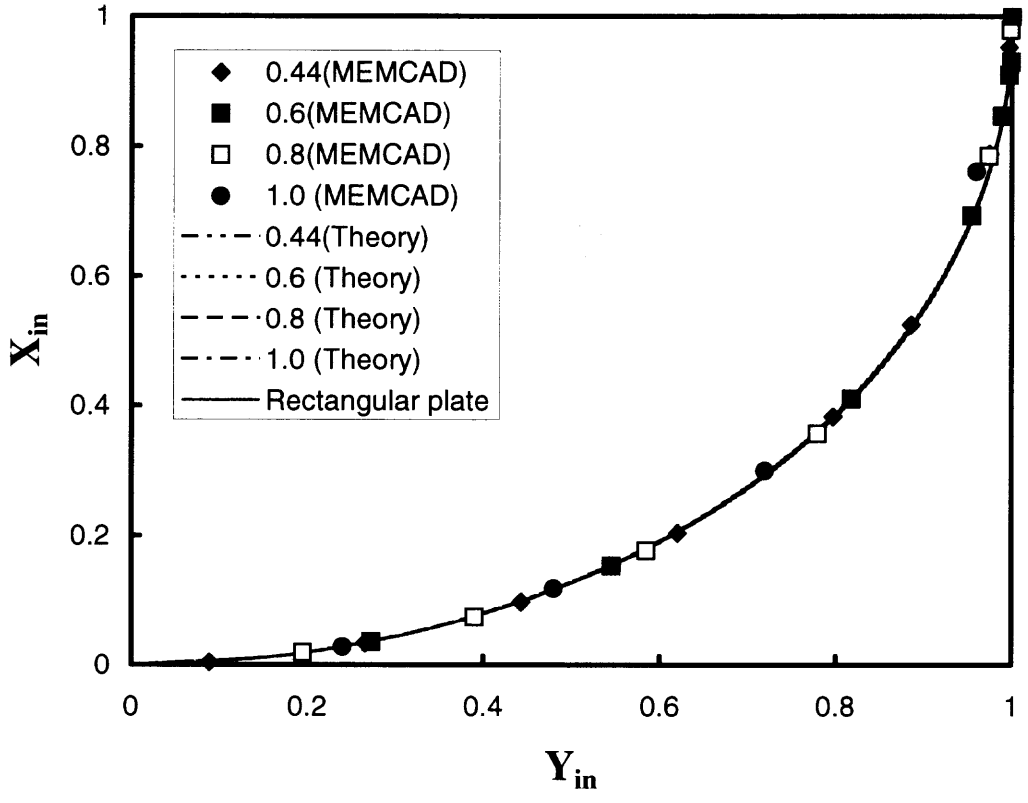

Figure 3.2 Comparison of analytical (equation 10, lines) and MEMCAD simulation (symbols) curves of X_{in} versus Y_{in} for an inner round plate actuator, with electrode length ratios β_i=0.44, 0.6, 0.8 and 1.0.

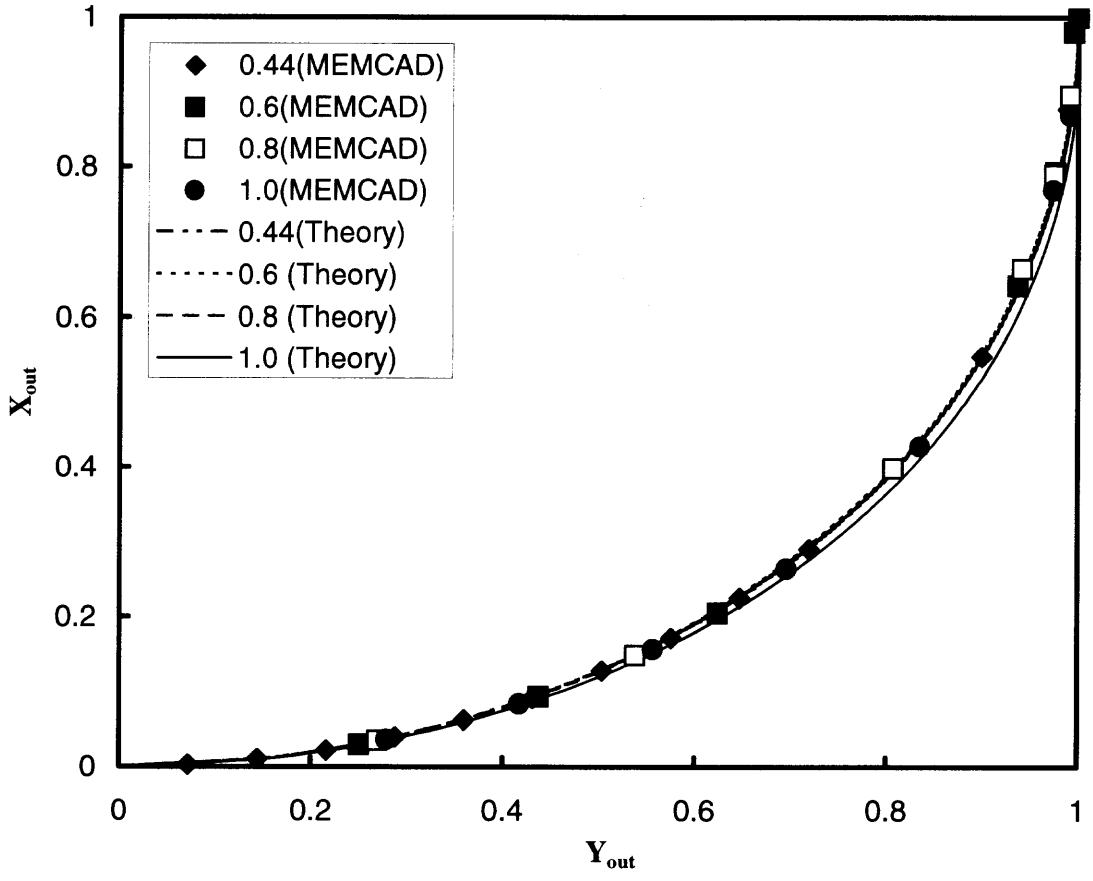

Figure 3.3 Comparison of analytical (Equation 15, lines) and MEMCAD simulation (symbols) curves of X_{out} versus Y_{out} for an outer ring plate actuator, with electrode length ratios β_o=0.44, 0.6, 0.8 and 1.0.

Table 3.1 Comparison of the fractional tilts at pull-in and the pull-in voltages at electrode length ratios β_i=0.44, 0.6, 0.8 and 1.0, using both MEMCAD simulations and the theoretical predictions of Equation 3.7 and 3.8. Actuator dimensions are: r=200μm, l_{in}=100μm, h=w=10μm, t_{in}=3μm and d=7μm

	r=200μm, l=100μm, h=w=10μm,t=3μm and d=7μm	
	β_i=0.44	β_i=0.60
θ_{pi}	1.0063 (equation 7) 0.9811 (MEMCAD)	0.7442 (equation 7) 0.7232 (MEMCAD)
Fractional difference of θ_{pi}	2.51%	2.82%
V_{pi}	114.78V (equation 8) 112.91V<V_{pi}<112.93V (MEMCAD)	74.3591 (equation 8) 73.38V<V_{pi}<73.40V (MEMCAD)
Fractional difference of V_{pi}	1.63%	1.32%
Meshing and convergence (MEMCAD)	27 node element node number: 9498 Convergence tolerance: 1×10^{-3}	27 node element node number: 12030 Convergence tolerance: 1×10^{-3}
$\beta_i\theta_{pi}$	0.4428 (equation 7) 0.4317 (MEMCAD)	0.4465 (equation 7) 0.4339 (MEMCAD)
	β_i=0.80	β_i=1.0
θ_{pi}	0.5684(equation 7) 0.5674 (MEMCAD)	0.4833(equation 7) 0.4761(MEMCAD)
Fractional difference of θ_{pi}	0.18%	1.49%
V_{pi}	51.3936 (equation 8) 51.33V<V_{pi}<51.35V (MEMCAD)	42.2250 (equation 8) 41.27V<V_{pi}<41.29V (MEMCAD)
Fractional difference of V_{pi}	0.12%	2.26%
Meshing and convergence (MEMCAD)	27 node element node number: 9522 Convergence tolerance: 1×10^{-3}	27 node element node number: 13728 Convergence tolerance: 1×10^{-3}
$\beta_i\theta_{pi}$	0.4547 (equation 7) 0.4539 (MEMCAD)	0.4833 (equation 7) 0.4761(MEMCAD)

Table 3.2 Comparison of the fractional tilts at pull-in and the pull-in voltages at electrode length ratios β_o=0.44, 0.6, 0.8 and 1.0, using both MEMCAD simulations and the theoretical predictions of Equation 3.13 and 3.14. Actuator dimensions are: r_1=300μm, r_2=500μm, l_{out}=100μm, h=w=10μm, t_{out}=3μm and d=7μm

	r_1=300μm, r_2=500μm, l=100μm, h=w=10μm,t=3μm and d=7μm	
	β_o=0.44	β_o=0.60
θ_{po}	0.9880(equation 13) 0.9985 (MEMCAD)	0.7089 (equation 13) 0.7153 (MEMCAD)
Fractional difference of θ_{po}	-1.06%	-0.90%
V_{po}	26.80 V(equation 14) 27.81V<V_{po}<27.83V (MEMCAD)	15.517 (equation 14) 16.02V<V_{po}<16.04V (MEMCAD)
Fractional difference of V_{po}	-3.79%	-3.21%
Meshing and convergence (MEMCAD)	27 node element node number: 12027 Convergence tolerance: 1×10^{-3}	27 node element node number: 14451 Convergence tolerance: 1×10^{-3}
$\beta_o\theta_{po}$	0.4347 (equation 13) 0.4394 (MEMCAD)	0.4254 (equation 13) 0.4292 (MEMCAD)
	β_o=0.80	β_o=1.0
θ_{po}	0.5340 (equation 13) 0.5129 (MEMCAD)	0.4580 (equation 13) 0.4480 (MEMCAD)
Fractional difference of θ_{po}	3.95%	2.19%
V_{po}	9.29 (equation 14) 9.30V<V_{po}<9.32 (MEMCAD)	7.35 (equation 14) 7.19<V_{po}<7.21V (MEMCAD)
Fractional difference of V_{po}	-0.026%	2.16%
Meshing and convergence (MEMCAD)	27 node element node number: 16458 Convergence tolerance: 1×10^{-3}	27 node element node number: 18090 Convergence tolerance: 1×10^{-3}
$\beta_o\theta_{po}$	0.4272 (equation 13) 0.4103 (MEMCAD)	0.4580 (equation 13) 0.4480(MEMCAD)

3.1.3 Summary

This chapter presented a systematic study of actuation and pull-in for round, double-gimbaled, electrostatic torsion actuators. It is found that for round plates, the fractional tilt at pull-in is only dependent on the electrode length ratio. For outer ring plates, the fractional deflection at pull-in is only dependent on the electrode length ratio and the ratio of the inner radius to the outer radius. The fractional tilts at pull-in are approximately equal to 1 (i.e., full actuator travel range) for both the inner round plate and the outer ring when electrode length ratios are equal to 0.44. Calculated pull-in and actuation results are verified by comparison with finite element MEMCAD simulations, with fractional difference found to be smaller than 4% for torsion mode dominant systems. It is concluded that the straightforward analytical approach provides a reasonable approximation to the more complex and time-consuming finite element analysis simulation method.

3.2 Rectangular Electrostatic Torsion Actuator

3.2.1 Theoretical Study

Figure 3.4 shows a schematic view of an electrostatic rectangular torsion actuator consisting of two identical springs, a movable plate and a stationary electrode. The horizontal distance from the center of the springs (i.e., the axis of rotation) to the nearest edge of the fixed electrode is a_1. a_2 and a_3 are the horizontal distances from the center of the springs to the end of the electrode and to the end of the movable plate, respectively. The electrode/plate width and vertical separation distance are b and d, respectively. The

length, width and thickness of each spring are l, w, and t, respectively. Before pull-in, the mechanical torque, M_m equals the electrostatic torque M_e [72], i.e.,

$$K_\alpha \alpha = \frac{\varepsilon_0 V^2 b}{2\alpha^2}\left[\frac{1}{1-\frac{\beta\alpha}{\alpha_{max}}} - \frac{1}{1-\frac{\gamma\alpha}{\alpha_{max}}} + \ln\left(\frac{\alpha_{max}-\beta\alpha}{\alpha_{max}-\gamma\alpha}\right)\right] \tag{3.17}$$

where α is the angle between the rectangular plate and the electrode, the maximum constrained tilt angle $\alpha_{max}=d/a_3$, the electrode length ratio $\beta=a_2/a_3$ and the reduced electrode edge location $\gamma=a_1/a_3$. V, ε_0 and K_α are the applied voltage, the dielectric constant of the vacuum, and the spring constant, respectively. In typical designs a_1 is much smaller than a_2 or a_3. Thus γ can be approximated as 0. This reduces Equation 3.17 to

$$K_\alpha \alpha = \frac{\varepsilon_0 V^2 b}{2\alpha^2}\left[\frac{1}{1-\frac{\beta\alpha}{\alpha_{max}}} - 1 + \ln\left(1-\frac{\beta\alpha}{\alpha_{max}}\right)\right] \tag{3.18}$$

At the pull-in point, the mechanical spring constant K_α (i.e., $dM_m/d\alpha$) is equal to the electrostatic spring constant (i.e., $dM_e/d\alpha$). Thus differentiating Equation 3.18 with respect to α, multiplying by α and subtracting Equation 3.18 yields

$$\frac{1}{1-\beta\theta_{pin}} - 1 + \ln(1-\beta\theta_{pin}) - \frac{\beta\theta_{pin}}{3(1-\beta\theta_{pin})^2} + \frac{\beta\theta_{pin}}{3(1-\beta\theta_{pin})} = 0 \tag{3.19}$$

where θ is the fractional deflection of the rectangular plate, α/α_{max}, and θ_{pin} is the fractional deflection at pull-in. Solving Equation 3.19 yields

$$\beta\theta_{pin} \cong 0.4404 \tag{3.20}$$

When the electrode length ratio $\beta=1$, $\theta_{pin}\cong 0.4404$, which means that the full plate electrode design gives about 44.04% travel range, a well-known result [64-68, 72]. When $\beta=0.4404$, $\theta_{pin}=1$, i.e., $\alpha=\alpha_{max}$. For lower electrode length ratios and a uniform gap depth, pull-in does not occur.

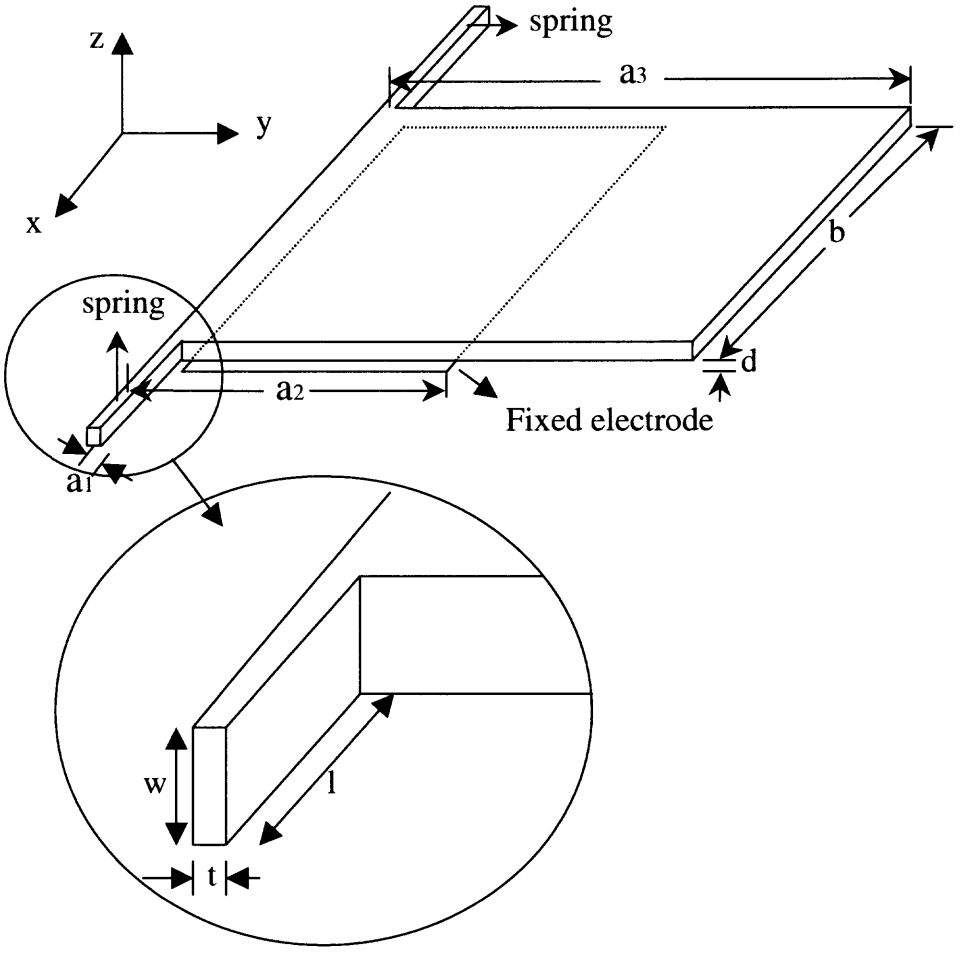

Figure 3.4 A schematic view of a rectangular electrostatic torsion actuator, consisting of tow springs, a movable rectangular plate, and a stationary electrode. a1 is the distance between the axis of torsion to the nearest edge of the electrode plate, a2 is the distance to the end of the plate, a3 is the distance to the end of the proof mass. d is the air gap depth and b is the width of the rectangular plate.

As shown by Degani, et al., [72], the pull-in voltage V_{pin} can be obtained from Equation 3.17:

$$V_{pin} = \sqrt{\frac{2K_\alpha d^3}{\varepsilon_0 a_3{}^3 b} \frac{\theta_{pin}{}^3}{\left[\frac{1}{1-\beta\theta_{pin}} - \frac{1}{1-\gamma\theta_{pin}} + \ln\left(\frac{1-\beta\theta_{pin}}{1-\gamma\theta_{pin}}\right)\right]}} \tag{3.21}$$

For typical designs where $\gamma \cong 0$ (i.e., the nearest edge of the rectangular electrode is close to the torsion spring) and $\beta\theta_{pin} \cong 0.4404$, the pull-in voltage expression in Equation 3.21 can be simplified as

$$V_{pin} \approx \sqrt{\frac{9.68K_\alpha \alpha^3{}_{pin}}{\varepsilon_0 b}} \tag{3.22}$$

where α_{pin} is the pull-in angle. Based on this equation, if the pull-in angle and voltage are set, there would be numerous combinations of K_α and b to satisfy the pull-in design. Note that in Equation 3.22 V_{pin} is expressed in terms only of the spring constant, the rectangular plate width and the specified pull-in angle. For completeness, note that α_{pin} can be written as:

$$\alpha_{pin} \approx 0.4404 \frac{d}{a_2} \tag{3.23}$$

and the pull-in voltage can be expressed as

$$V_{pin} \approx 0.909 \sqrt{\frac{K_\alpha d^3}{\varepsilon_0 b a_2{}^3}} \tag{3.24}$$

Additional design generalizations can be made by normalizing the applied voltage and resulting tilt angle by their respective pull-in values in Equation 3.18 and 3.22. Thus taking $X=\alpha/\alpha_{pin}$ and $Y=V/V_{pin}$, the equations become to:

$$\frac{Y^2}{X^3}\frac{\left[\frac{1}{1-0.44X}-1+\ln(1-0.44X)\right]}{0.2065}\cong 1 \tag{3.25}$$

$$V_{\alpha,X}\approx Y\sqrt{\frac{9.68K_\alpha\alpha^3}{\varepsilon_0 bX^3}} \tag{3.26}$$

Equation 3.25 is a general structural equation for electrostatic torsion actuators with rectangular plates. It shows that the relationship between the normalized applied voltage and the normalized tilt angle is independent of the spring parameters, the rectangular plate width and length, the air gap depth and the electrode length and width if the nearest edge of the electrode under the rectangular plate is close to the torsion spring. In Equation 3.26, $V_{\alpha,X}$ is the required applied voltage for tilt angle α at working point X. If α is fixed at a maximum desired value, designers can select different working points to realize a particular actuation. For instance, X=0.9 can be used to avoid the bad controllability at the pull-in point X=1.0. Then the voltage corresponding to α at X can be obtained. Note that in equation (3.26) $V_{\alpha,X}$ is expressed in terms only of the spring constant, the rectangular plate width, the specified angle, the normalized applied voltage and the normalized tilt angle.

Based on Equation 3.20, 3.25 and 3.26, a straightforward design approach can be developed in which only simple calculations are needed for the full design of a rectangular electrostatic torsion actuator. Figure 3.5 shows a schematic view of the approach. In this figure, $\otimes_\alpha$ is the resonant frequency for the torsion mode. The resonant frequency $\otimes_\alpha$ is determined by

$$f_\alpha=\frac{1}{2\pi}\sqrt{\frac{K_\alpha}{I_\alpha}} \tag{3.27}$$

where I_α is the mass moment of inertia about the rotation axis, which can be written as

$$I_\alpha = \iiint \rho(y^2 + z^2)dxdydz \approx \frac{1}{3}\rho a_3 bw(a_3^{\,2} + w^2) \tag{3.28}$$

where ρ is the material density. When t<w, the spring constant can be written as

$$K_\alpha = \frac{2}{3}G\frac{wt^3}{l}\left[1 - \frac{192t}{\pi^5 w}\sum_{n=1,3,5\ldots}\frac{1}{n^5}\tanh\left(\frac{n\pi w}{2t}\right)\right] \tag{3.29}$$

where G is the shear modulus and equals 0.73×10^{11}Pa for silicon [75].

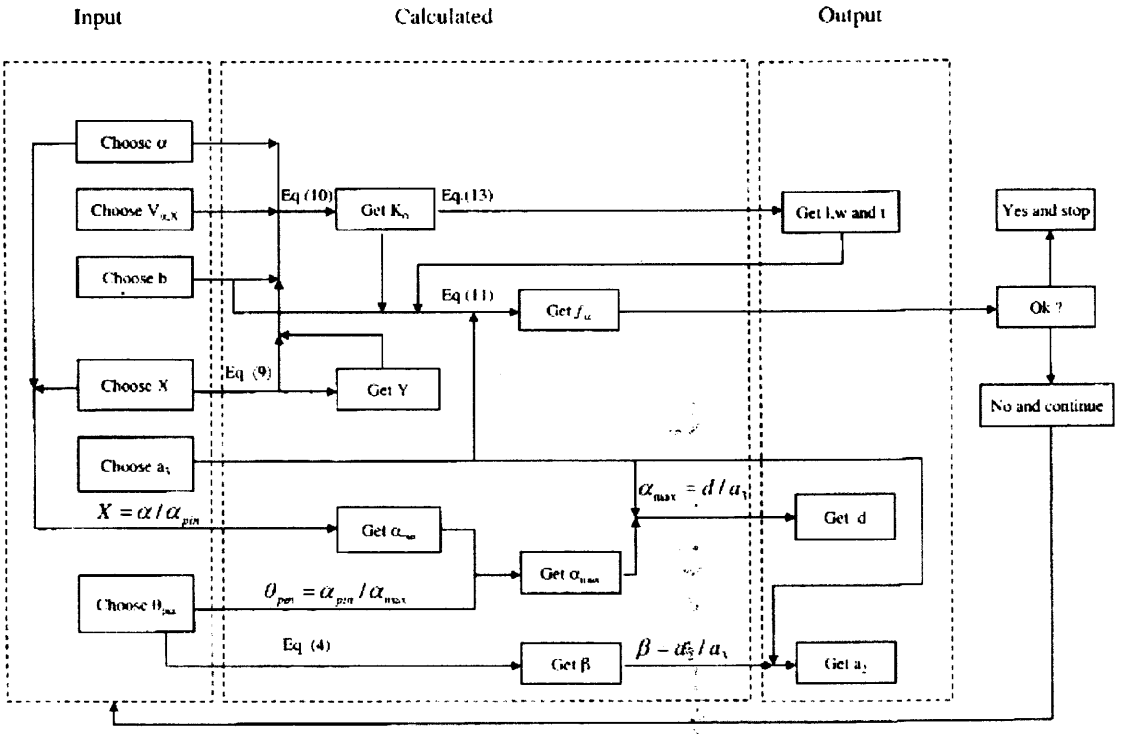

Figure 3.5 A schematic view of the design principle. The tilt angle α, the applied voltage $V_{\alpha, X}$, the rectangular plate width b, the working point X, the air gap depth d (or the rectangular plate length a_3) and the fractional deflection at pull-in θ_{pin} are the input parameters. The spring parameters, the rectangular plate length or gap depth, the electrode length a_2 and the torsion mode resonant frequency are the output parameters.

Referring to Figure 3.5, if the desired maximum controllable tilt angle α, the working point X, and the required applied voltage $V_{\alpha,X}$ are set by the designer, the spring constant can be obtained after choosing the rectangular plate width b. Then, the designer can choose the spring length, width and thickness based on the spring constant equation, the desired resonant frequency and practical fabrication considerations. With α and X, the pull-in angle α_{pin} can be obtained. After choosing the fractional deflection at pull-in θ_{pin}, both the electrode length ratio β, and the maximum constrained tilt angle α_{max} can be calculated. Specifying one of either the plate length a_3 or electrode spacing d allows the other to be determined. Using β and a_3, the electrode length a_2 can be obtained. Finally, by combining b, a_3 and the spring constant, the torsion mode resonant frequency, $\otimes_\alpha$, can be calculated. If the value of $\otimes_\alpha$ is acceptable, then the design procedure stops. Otherwise, redesign is needed.

3.2.2 Verification

To verify the simplified approach to actuator design outlined in Figure 3.5, we compare the results of the key calculations in Equation 3.20, 3.22, 3.25, and 3.26 individually with results from both full analytical calculations and MEMCAD simulations using typical design parameters. Four different devices are considered during the verification process. Their dimensions are listed in the table 3.3.

Device 1 in Table 3.3 is used for the verification of Equation 3.20. For this device, Table 3.4 shows the calculated fractional deflection at pull-in θ_{pin}, and the product of θ_{pin} with the electrode length ratio β for three values of β, 0.4404, 0.75 and 1. These results have been determined using both the full analytical calculation (a) and MEMCAD

version 4.8 simulation (M). As predicted in equation (3.20), $\beta\theta_{pin}$ is always approximately equal to 0.44. The MEMCAD meshing and convergence parameters are listed in the table.

Table 3.3 Design parameters for the devices used to verify the main results of the theoretical study

	l(μm)	w(μm)	t(μm)	a_3(μm)	b(μm)	d(μm)	a_2(μm)
Device 1	100	10	3	200	300	10	Variable, $a_2=a_3\beta$
Device 2	100	10	3	300	300	20	300
Device 3	200	20	3	400	400	25	250
Device 4	100	10	3	408.6	300	15	224.7

Devices 1 (with β=0.75) and 2 in Table 3.3 are used to verify the result from Equation 3.22. The plate width and spring parameters of these two actuators are the same, however, the plate length and gap depth are different. Table 3.5 confirms that pull-in voltages are roughly the same at the same pull-in angle α_{pin} for the two devices, as predicted in Equation 3.22.

Table 3.4 The calculated fractional deflection θ_{pin}, and the product of θ_{pin} and the electrode length ratio β for different values of β, 0.4404, 0.75 and 1, for device 1

	θ_{pin}	$\beta\theta_{pin}$
β=1	0.4404(64.42V)(a) 0.4381(65.41V)(M) Meshing and convergence (M): • 27 node element • node number: 10608 • V_{pin} convergence range: 65.41V<V_{pin}<65.43V • Convergence tolerance: 1×10^{-3}	0.4404(a) 0.4381(M)
β=0.75	0.5872(99.18V)(a) 0.5733(99.16V)(M) Meshing and convergence (M): • 27 node element • node number: 13536 • V_{pin} convergence range: 99.16V<V_{pin}<99.18V • Convergence tolerance: 1×10^{-3}	0.4404(a) 0.4300(M)
β=0.4404	1.00005(220.41V)(a) 0.9843(216.04V)(M) Meshing and convergence (M): • 27 node element • node number: 10974 • V_{pin} convergence range 216.04V<V_{pin}<216.05V • Convergence tolerance: 1×10^{-3}	0.4404(a) 0.4335(M)

Devices 2 and 3 in Table 3.3, with completely different design parameters, are used to verify the relationship described in Equation 3.25. Figure 3.6 plots analytical and MEMCAD solutions of X versus Y for devices 2 and 3 along with Equation 3.25. The curves are nearly indistinguishable, thus confirming Equation 3.25.

Table 3.5 Pull-in voltages and angles for devices 1 and 2, determined using full analytical calculations (a) and MEMCAD simulations (M). The two devices have different rectangular plate length, air gap depth and electrode length ratio, but they have the same spring parameters and rectangular plate width. The pull-in voltages are almost the same at the same pull-in angle.

	V_{pin}(V)	α_{pin}(°)
Device 1 (β=0.75)	99.18(a) 99.16V<V_{pin}<99.18V(M) Meshing and convergence (M): • 27 node element • node number: 13536 • Convergence tolerance: 1×10^{-3}	1.6830(a) 1.6418(M)
Device 2(β=1.0)	99.18V(a) 100.66V<V_{pin}<100.68V(M) Meshing and convergence (M): • 27 node element • node number: 12836 • Convergence tolerance: 1×10^{-3}	1.6835(a) 1.6925(M)

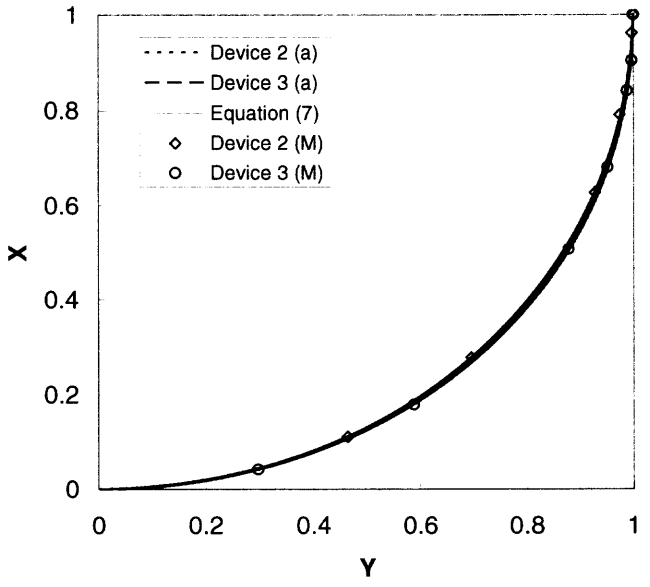

Figure 3.6 Curves of X versus Y for devices 2 and 3 determined using analytical calculations, MEMCAD simulations and Equation 3.25. X is the ratio of the tilt angle to pull-in angle. Y is the ratio of the applied voltage to pull-in voltage. For the MEMCAD simulation of device 3, a 27-node element was used for structure meshing. The node number is 8478 and the convergence tolerance is 1×10^{-3}. The pull-in voltage by the design approach is 166.73V and the pull-in voltage by MEMCAD is $99.16V<V_{pin}<99.18V(M)$. The pull-in angle by the design approach is 2.525°, and the pull-in angle by MEMCAD is 2.537°.

Devices 2 and 4 in Table 3.3 are used to verify the relationship in Equation 3.26. Table 3.6 shows the calculation and simulation results for the two structures with different rectangular plate length and air gap depth, but with the same plate width and spring parameters. Device 4 is designed using the approach in Figure 3.5 to operate identical to Device 2, at the same working point X=0.8, with the same maximum controllable tilt angle $\alpha=1.3435°$ and the same applied voltage $V_{\alpha,X}\cong97.5V$. This behavior is confirmed by the simulation and calculation results. By comparing the analytical and MEMCAD simulation results, for example, the values of $\beta\theta_{pin}$ in Table 3.4,

the values of V_{pin} and α_{pin} in Table 3.5, the values of Y(X) in Figure 3.6 or the values θ_{pin} and α_{pin} in Table 3.6, the fractional difference is generally found to be smaller than 3%.

Table 3.6 The simulation results for two structures with different rectangular plate length and air gap depth, but with the same rectangular plate width and spring parameters. At X=0.8, the applied voltage $V_{\alpha,X}$, is approximately equal to the values determined using Equation 3.26

	Device 2		Device 4		Equation 3.26
X	0.8(a)	0.7591(M)	0.8(a)	0.7827(M)	0.8
Y	0.982	0.9686(M)	0.982	0.9788(M)	0.982
$\alpha(°)$	1.3436(a)	1.2848(M)	1.3435(a)	1.3149(M)	1.3435
$V_{\alpha,X}(V)$	97.4(a)	97.5(M)	97.4(a)	97.5(M)	97.5
θ_{pin}	0.4404(a)	0.4429(M)	0.8(a)	0.7985(M)	
$\alpha_{pin}(°)$	1.6835(a)	1.6925(M)	1.6835(a)	1.6800(M)	
$\alpha_{max}(°)$	3.821		2.104		
β	1		0.55		
$V_{pin}(V)$	99.18(a)	100.66V<V_{pin}<100.68V(M)	99.21(a)	99.61V<V_{pin}<99.65V(M)	
	Meshing and convergence (M): • 27 node element • node number: 12836 • Convergence tolerance: 1×10^{-3}		Meshing and convergence (M): • 27 node element • node number: 9876 • Convergence tolerance: 1×10^{-3}		

3.2.3 Example Application

As an example application, we wish to design an actuator that has a maximum controllable tilt angle $\alpha=1°$ at working point X=0.95 and applied voltage $V_{\alpha,X}=48V$. For this specific application, we choose a plate width b=0.7mm, a plate length $a_3=0.7mm$, and a fractional deflection at pull-in $\theta_{pin}=1$. Following the procedure of Figure 3.5, the

required spring constant is found to be $K_\alpha=2.405\times10^{-7}$N·m. Practical fabrication considerations and the desire for a very flat plate surface require the spring width to be w=50μm and spring thickness t=5μm, thus the spring length l=1185μm. A folded spring can be used to achieve this length. The resulting resonant frequency f_α is found to be 806Hz. The pull-in angle $\alpha_{pin}\cong1.053°$, the electrode length ratio $\beta\cong0.4404$, $\alpha_{max}\cong1.053°$, $d\cong12.9\mu m$ and $a_2\cong308\mu m$.

To compare the design results with a fabricated device, a full plate actuator with $\beta=1$ is also considered. A full plate actuator is easy to construct because the silicon substrate can be used as the fixed electrode. Using the design approach of Figure 3.5, for this device $\alpha_{pin}\cong0.464°$ and $V_{pin}=14.18V$. At working point X=0.95, $\alpha\cong0.44°$, $V_{\alpha,X}=14.16V$. Figure 3.7 shows an optical profilometry image of this device biased at pull-in. The image was measured using a VEECO NT 3300 system. Fabrication was accomplished using deep reactive ion etching and ultra thin wafer bonding technology [99]. The finished device differs slightly from the design, having a measured gap depth of 11.2 μm instead of 12.9μm.

Figure 3.8 shows the actuated angle and fractional deflection versus applied voltage, as measured using the profilometer. The fractional deflection near pull-in is 43.75% at V=11.75V which is very close to the theoretical value of 44.04% at a calculated pull-in voltage of 11.47V for d=11.2μm. Note that $\alpha(0V)=0.0463°$, which is the result of the gravity force. This value is very close to the theoretical prediction of 0.0466°.

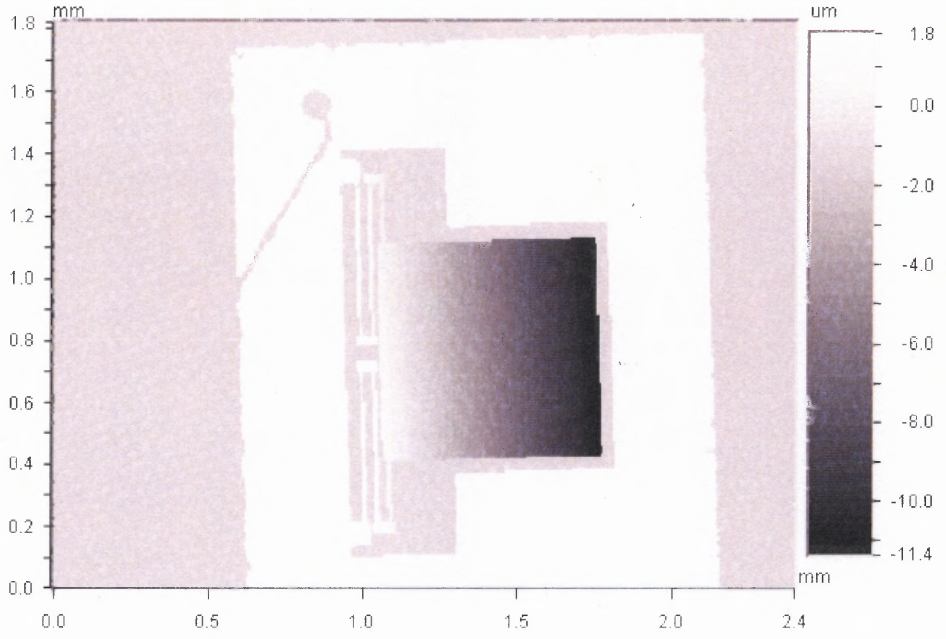

Figure 3.7 Optical profilometry image of a fabricated, full-plate torsion actuator under test. The applied voltage is 11.85V and the movable plate is snapped down to the bottom electrode. (w=50μm, t=5μm, l=1185μm, a_3=700μm, b=700μm, d= 11.2μm and β=1)

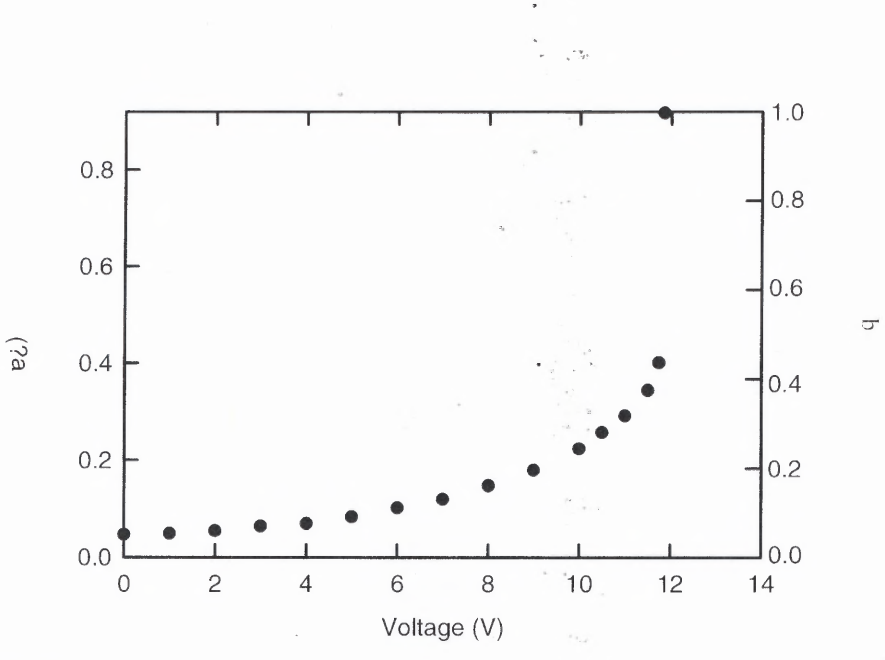

Figure 3.8 Measured tilt angle α and fractional deflection versus applied voltage for the actuator in Figure 3.7.

3.2.4 Limitations of the Theory

The theory and the equations used in this chapter have not considered 1) spring stiffening, 2) fringing fields, and 3) the effect of bending mode actuator movement. Also, in the calculation, the angle α is approximately treated as $\tan(\alpha)$. This will give rise to less than 1% error even at 10°. Of the limitations, the bending mode effect will most strongly affect the application range of the theory.

In order to get a large tilt angle at a reasonably low applied voltage, the springs need to be as long and thin as possible for a given plate thickness. However, if the springs are too long, the resulting electrostatic force induced bending mode movement will decrease the effective gap depth between the electrodes, decreasing both the pull-in angle and voltage.

For a double clamped structure, the spring constant of the bending mode K_z can be written as

$$K_z = \frac{192EI}{(2l)^3} = \frac{3}{2}\frac{Ew^3t}{l^3} \tag{3.30}$$

where E is the Young's modulus in the direction of bending mode. In this paper, E is 1.31×10^{11}Pa for (100) silicon [75]. K_z decreases with l^{-3}, whereas K_α decreases with l^{-1}. The resonant frequency of the bending mode f_z can be written as

$$f_z = \frac{1}{2\pi}\sqrt{\frac{K_z}{m}} \tag{3.31}$$

where m is the mass of the suspended structure.

To illustrate the effects of spring length on bending mode movement, and its impact on the simplified design approach of the paper, we have designed three devices A, B, and C, with target pull-in angles of 2.98, 3.90 and 4.38 degrees, respectively, at 100 V.

Only the spring length and gap depth vary. Table 3.7 shows the pull-in angle and the pull-in voltage for these three devices determined using both the design approach of the paper and MEMCAD simulations. Notice that the MEMCAD results predict serious decreases in the pull-in angle and voltage for the longer springs of Devices B and C.

Table 3.7 Pull-in angles and pull-in voltage for three devices determined using the design approach of this study (d) and MEMCAD simulations (M). The design pull-in voltage is 100 V for three different design pull-in angles. The spring length and gap depth vary for each design

	Device A w=10μm, t=2μm, a_3=200μm, a_2=88.08μm, b=300μm	Device B w=10μm, t=2μm, a_3=200μm, a_2=88.08μm, b=300μm	Device C w=10μm, t=2μm, a_3=200μm, a_2=88.08μm, b=300μm
	l=174.8μm, d=10.4μm	l=390.9μm, d=13.6μm	l=552.8μm, d=15.3μm
$\alpha_{pin,\,d}(°)$ (design)	2.98	3.90	4.38
$\alpha_{pin,\,M}(°)$ (MEMCAD)	2.87	3.23	3.08
$V_{pin,\,d}(V)$ (design)	100	100	100
$V_{pin,\,M}(V)$ (MEMCAD)	95.41 V<V_{pin}<95.43V	86.45V<V_{pin}<86.46V	79.16V<V_{pin}<76.18V
	Meshing and convergence (M): • 27 node element • node number: 7932 • Convergence tolerance: 1×10^{-3}	Meshing and convergence (M): • 27 node element • node number: 12018 • Convergence tolerance: 1×10^{-3}	Meshing and convergence (M): • 27 node element • node number: 8430 • Convergence tolerance: 1×10^{-3}

A measure of the importance of the bending mode compared to the torsion mode can be obtained by calculating the resonant frequencies for each mode. Table 3.8 shows f_α, f_z, f_α/f_z and fractional differences in pull-in angle and voltage using MEMCAD and the theory in this study for devices 1(β=0.75), 2, 3, 4, A, B and C. Notice that the fractional differences in pull-in angle and pull-in voltage are generally small (<3%) when the ratio of the resonant frequency of the torsion mode to that of the bending mode, f_α/f_z, is small (<0.1). For devices A, B and C, with longer springs that are more prone to bending, the fractional differences and the value of f_α/f_z become large. The fractional differences for device C exceed 20%. From the simulation results in Tables 3.7 and 3.8, it is concluded that a pull-in angle of 4° would be difficult to obtain with w=10μm, t=2μm, a3=200μm, and b=300μm. In general, the design approach of this study is useful only for actuators in which the torsion mode is dominant. For the designs that are considered, it is found that for f_α/f_z<0.1, the fractional difference between analytical calculations and MEMCAD simulations is <3%.

Table 3.8 Calculated torsion and bending mode resonant frequencies for the different devices considered in this study, and fractional differences in pull-in angle and voltage determined using the design approach (d) and MEMCAD simulations (M).

	Device 1 (β=0.75)	Device 2	Device 3	Device 4	Device A	Device B	Device C
f_α (KHz)	12.0	6.55	4.159	4.12	5.137	3.435	2.889
f_z (KHz)	119.0	97.1	59.4	83.2	42.0	12.6	7.468
f_α/f_z	0.101	0.0675	0.07	0.0495	0.122	0.273	0.387
$(\alpha_{pin,d}-\alpha_{pin,M})/\alpha_{pin,d}$	2.45%	-0.53%	-0.47%	0.21%	3.69%	17.18%	29.68%
$(V_{pin,d}-V_{pin,M})/V_{pin,d}$	0.02%	-1.49%	2.42%	-0.40%	4.59%	13.55%	20.84%

3.2.5 Summary

This chapter has presented several basic equations to describe rectangular electrostatic torsion actuators, which may give designers a better understanding of their performance. Based on these equations, a straightforward, angle based design approach has been proposed, which can avoid time consuming simulations. The results have been verified by comparing them with analytical calculations and MEMCAD simulations with fractional difference smaller than 3% for torsion mode dominant actuators. Also, good agreement is found by comparison with the measured behavior of a microfabricated full-plate device.

CHAPTER 4

VARIABLE CAPACITOR

4.1 Design and Theory

4.1.1 Variable Capacitor with Parallel Plate Drive Electrodes

Figure 4.1 shows a simplified electrical/mechanical schematic of a variable capacitor and LC drive circuit. The device consists of sets of fixed and movable vertical plates, forming separate drive and sense capacitors. The drive capacitor can consist of either parallel plate or comb drive electrodes, with each approach having attending benefits. The parallel plate drive electrode approach is straightforward and reliable. The comb drive electrode approach may have lower drive voltage and better linearity. In the parallel plate drive devices, C_d, the drive capacitor, has an electrode spacing that is three times that of C_s, the sense capacitor. Figure 4.2 shows several microscope images of the fabricated parallel plate drive device. In Figure 4.2a, two separate drive capacitors are placed symmetrically on the ends of the structure, and the sense capacitor occupies the center region. The sense and drive capacitors share a common electrode E_p, which is connected through four folded springs to a movable support beam with attached fingers. A portion of a folded spring is shown in Figure 4.2b. As shown in Figure 4.2c and 4.2d, C_d and C_s actually consist of wide and narrow air gap capacitances. In both cases, the net capacitance is strongly dominated by the narrow gap capacitor. The narrow drive gap spacing is designed to be three times that of the narrow sense gap so that a maximum sense electrode displacement can be achieved at the lowest possible applied voltage without causing drive electrode pull-in. The 2.8μm long bumpers in Figure 4.2c, which are

always at the same potential, limit the maximum displacement to less than the full 3μm sense gap distance. Before the electrode E_p contacts the bumpers, the capacitance increases parabolically with increasing applied voltage. After contact, the capacitance increases approximately linearly. This is similar to a previous report in [93] where curved electrode actuators were used to extend the travel range.

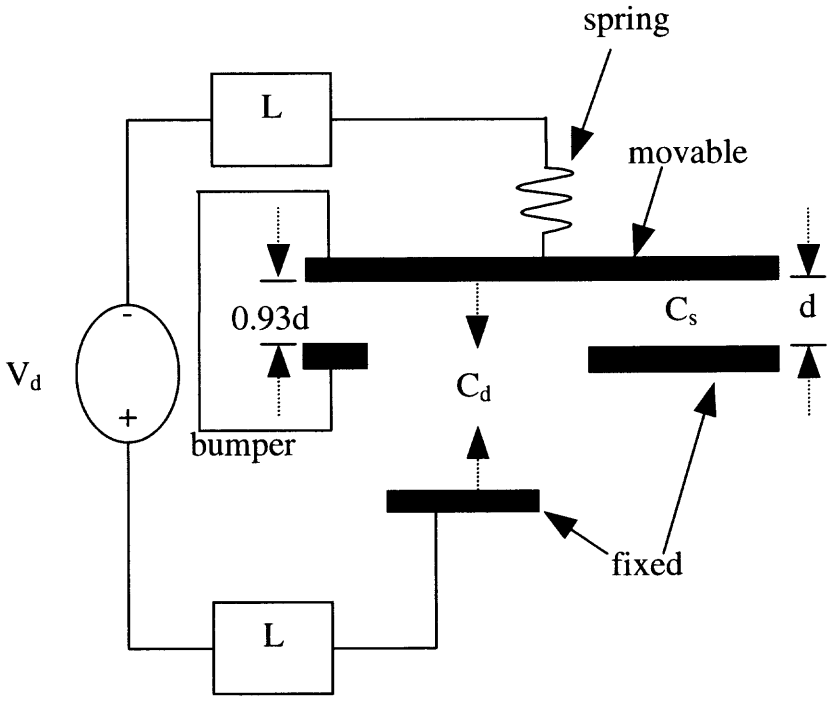

Figure 4.1 Simplified electrical/mechanical schematic of micromachined variable capacitor and LC drive circuit. In the parallel plate drive device, C_d, the drive capacitor, has an electrode spacing that is three times that of Cs, the sense capacitor. L is about 0.1 mH.

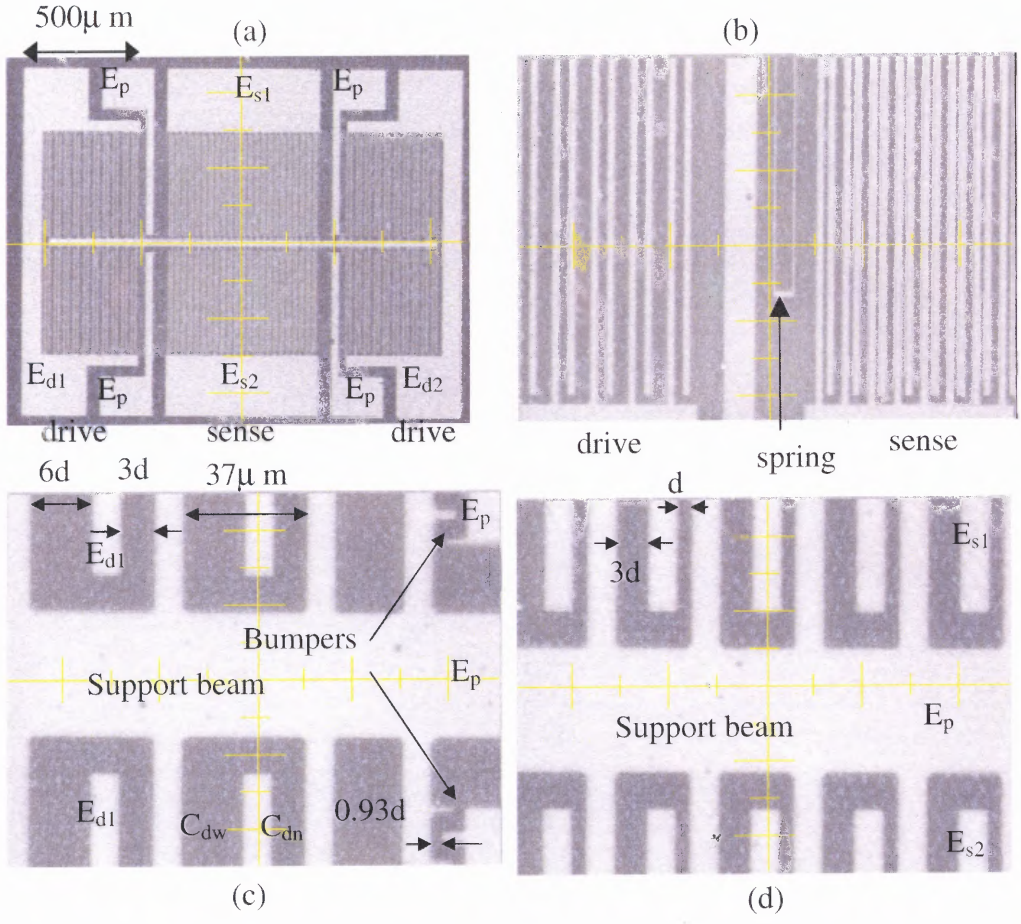

Figure 4.2 Microscope images of the fabricated parallel capacitor drive device. (a) Top view of fabricated device. The drive voltage is applied between the common electrode E_p and the drive electrodes E_{d1} and E_{d2}. The capacitance is sensed between Es (shorted E_{s1} and E_{s2}) and the common electrode E_p. The movable fingers are mounted to a center support beam and connected to the E_p electrodes by 4 μ m wide, 730 μ m long, 29.5 μ m thick springs. (b) Close up image showing a portion of the folded spring. (c) Close up image of drive capacitor showing placement of movable fingers with smallest asymmetric electrode spacing 3d=9 μ m and bumper spacing nominally 0.93d=2.8 μ m. The bumpers are always at the same potential. (d) Close up image of sense capacitor showing smallest electrode spacing d=3.0μm.

The voltage for transition from parabolic to linear behavior can be estimated analytically by calculating the drive electrode pull-in voltage, V_{pin}. Balancing the electrostatic and mechanical forces before pull-in gives

$$\frac{\varepsilon_0 V^2 A}{2(d_0 - \Delta d)^2} - \frac{\varepsilon_0 V^2 A}{2(Nd_0 + \Delta d)^2} = k\Delta d \tag{4.1}$$

where N is the wide to narrow gap spacing ratio for the drive electrode, (N.B., N>1) and Δd is the displacement. A, ε_0, V and k are the capacitor area, permittivity of free space, applied voltage and spring constant, respectively. An expression for the fractional displacement at pull-in, $x=\Delta d_{pin}/d_0$, is found by maximizing Equation 4.1. Thus differentiating it with respect to displacement, multiplying by Δd, and subtracting it, gives

$$\frac{1-3x_{pin}}{(1-x_{pin})^3} - \frac{N+3x_{pin}}{(N+x_{pin})^3} = 0 \tag{4.2}$$

where the normalized displacement at pull-in depends only on N. Figure 4.3 shows a plot of x_{pin} versus N. Observe that x_{pin} decreases dramatically as N approaches 1. For example, at N=2, x_{pin}=0.3069. When N is infinite, x_{pin}=1/3, which is the well-known result for a single parallel plate system.

By substituting x_{pin} into Equation 4.1, the pull-in voltage can be written as

$$V_{pin} = \sqrt{\frac{x_{pin}}{\frac{1}{(1-x_{pin})^2} - \frac{1}{(N+x_{pin})^2}} \frac{2d_0^3 k}{\varepsilon_0 A}} \tag{4.3}$$

As discussed in the fabrication and results section, the analytical results can be compared with simulation results obtained using MEMCAD (now COVENTOR) finite

element analysis software. Using this tool, the spring constant and resonant frequency for the system is estimated to be about 13 N/m and 3.01KHz, respectively.

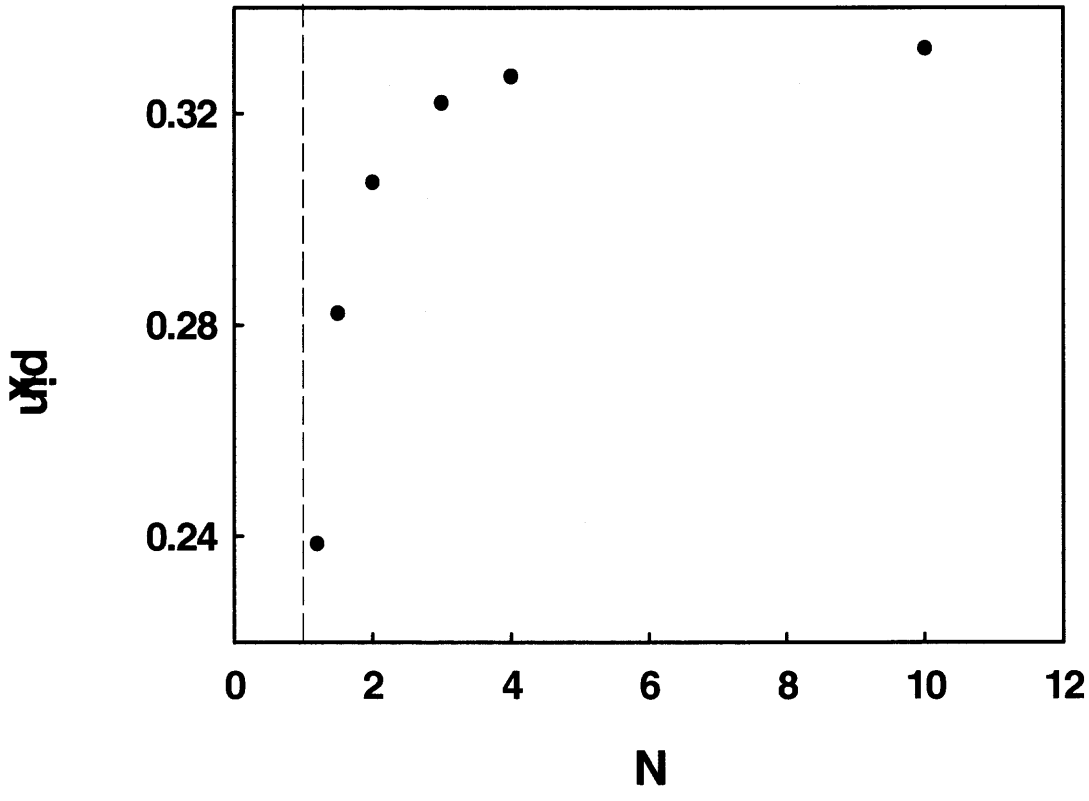

Figure 4.3 Fractional displacement at pull-in, x_{pin}, versus drive electrode wide to narrow gap spacing ratio, N>1, for parallel plate capacitor drive.

4.1.2 Variable Capacitor with Comb Drive Electrodes

Figure 4.4 shows a schematic drawing of a lateral comb-drive structure. The displacement of this structure is parallel to the substrate (in the x-y plane). When a voltage difference V is applied between the two comb electrodes, the electrostatic force F_e pulls the electrodes toward each other.

To calculate the electrostatic force, it is assumed that the ground-plane under the structure is floating and that the electrode overlap l_c is large compared to the electrode spacing d_c, width w_c and height h_c. In this case fringe fields at the electrode ends do not change significantly with l_c and give a negligible contribution to the electrostatic force. Under these assumptions, the capacitance consists of two simple plane-plate capacitors and a capacitor resulting from the fringe fields, which can be calculated using conformal mapping [94], and can be approximated by [95, 96].

$$C = 2N\varepsilon_0 l_c \left(\frac{h_c}{d_c} + \frac{1}{\pi} \ln \left\{ \left[\left(\frac{w_c}{d_c} + 1 \right)^2 - 1 \right] \left(1 + \frac{2d_c}{w_c} \right)^{1+\frac{w_c}{d_c}} \right\} \right) \tag{4.4}$$

where N denotes the number of the movable electrodes, and ε_0 is the permittivity of free space.

Thus the lateral electrostatic force F_e in response to an applied voltage V can be written as

$$F_e = -\frac{V^2}{2}\frac{\partial C}{\partial l_c} = -V^2 N\varepsilon_0 \left(\frac{h_c}{d_c} + \frac{1}{\pi} \ln \left\{ \left[\left(\frac{w_c}{d_c} + 1 \right)^2 - 1 \right] \left(1 + \frac{2d_c}{w_c} \right)^{1+\frac{w_c}{d_c}} \right\} \right) \tag{4.5}$$

The displacement due to this force is

$$\Delta l_c = \frac{F_e}{k} \tag{4.6}$$

where by design, the comb drive spring constant is about 13N/m, the same as that for the parallel plate drive device discussed above.

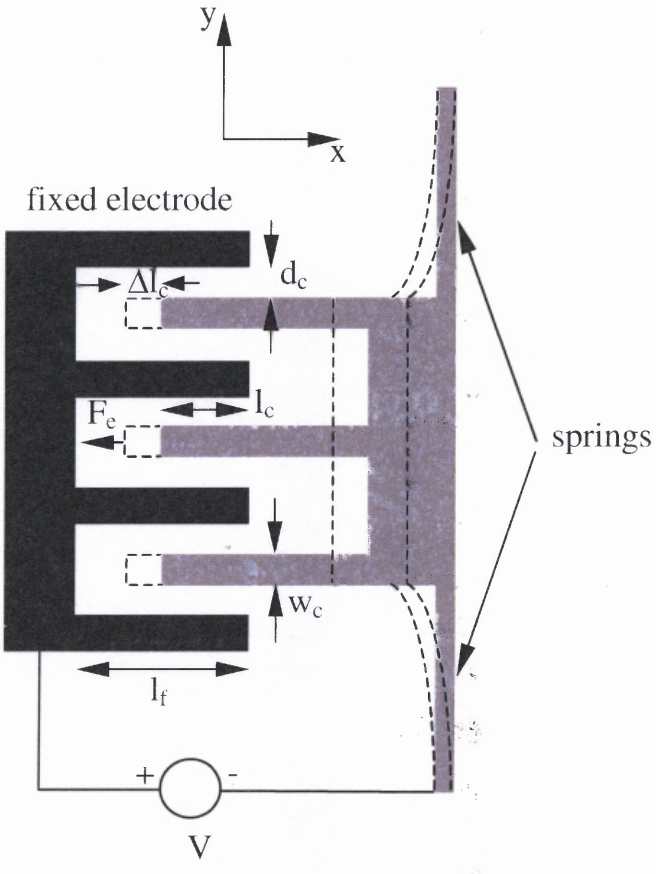

Figure 4.4 A schematic drawing of a lateral comb-drive structure with finger length l_f, overlap distance l_c, finger width w_c and electrode spacing d_c. The movable electrode spring constant is k_c and the electrode moves a lateral distance Δl_c in response to an applied electrostatic force F_e. Not shown in the figure, the electrodes extend a depth h_c in the z direction.

Figures 4.5(a), (b), (c), and (d) show several microscope images of the fabricated device with comb capacitor drive. Other than using comb drive electrodes, the device is the same as the parallel plate drive device in Figure 4.2. The design parameters for the comb drive device are: l_c=5μm, w_c=3μm, d_c=3μm, and the comb finger length and height are l_f=11μm and h_c=30μm, respectively. The designed travel response is 2μm with 14V applied on the two drive electrodes, which would be expected to give a 200% capacitance change. The designed resonant frequency is 3.0KHz.

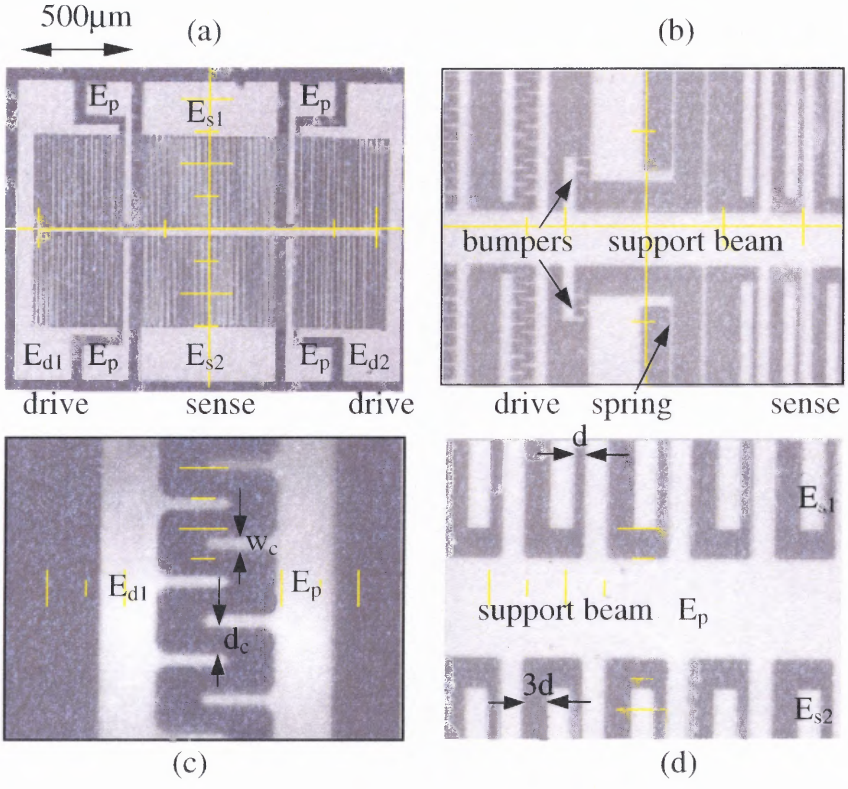

Figure 4.5 Microscope images of the fabricated device with comb capacitor drive. (a) Top view of fabricated device. (b) Close up image showing a portion of the folded spring, comb drive capacitor, parallel sense capacitor, and the bumper. (c) Close up image showing a portion of the comb drive capacitor. (d) Close up image showing a portion of the parallel sense capacitor.

4.2 Fabrication and Results

Figure 4.6 shows the main fabrication steps. The process starts with SU-8 photolithography on an oxidized silicon wafer to form a cavity. The realized cavity depth is about 22μm at 3000 rpm. An ultra thin silicon wafer [97] was bonded to the silicon substrate by SU-8 bonding [98] at 105°C, using an EVI 501 universal bonding system. Aluminum was then sputtered onto the bonded wafer stack, and patterned by HP_3O_4 etching at 40° after photolithography. The devices were released by deep reactive ion etching (DRIE) using the BOSCH process in a Unaxis/Plasma-Therm inductively coupled plasma system. Finally, the photoresist was removed using oxygen plasma etching. The aluminum on the structure, besides allowing good external electrical contact, also decreases the device series resistance, improving its Q factor.

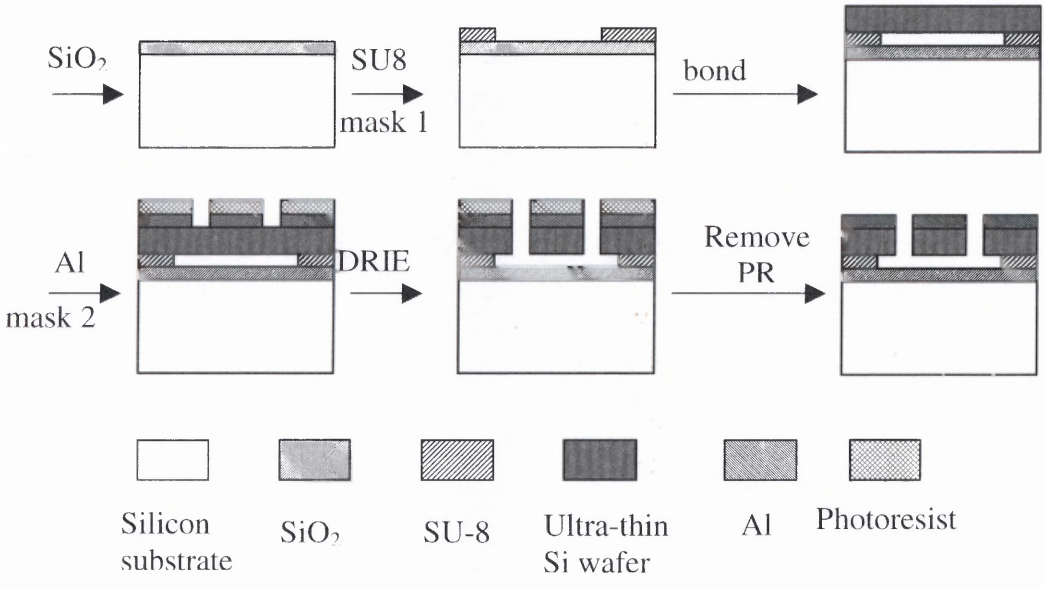

Figure 4.6 Two-mask processes schematic for micromachined variable capacitor.

Figure 4.7 shows the capacitor sidewall image using a VEECO NT3300 optical profilometer. It shows that the ultra-thin silicon wafer is approximately 29.5μm thick. In addition, the image reveals the capacitor surface microroughness induced by the Bosch etching process. The RMS roughness is about 71nm.

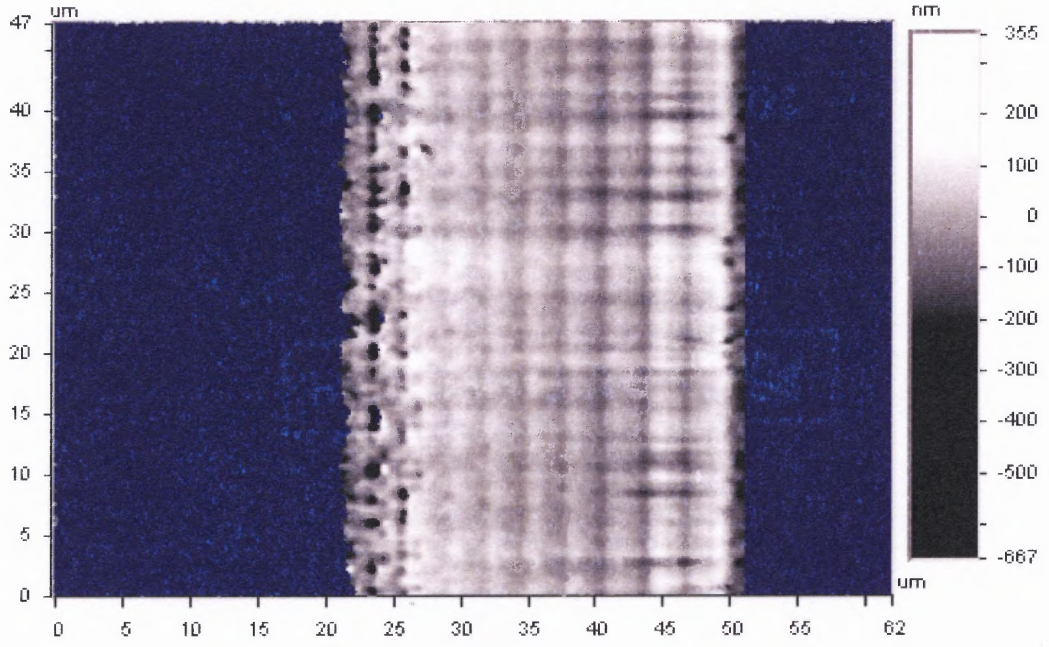

Figure 4.7 Optical profile of device sidewall after DRIE etching.

Figure 4.8 shows sense capacitor photos at 0V, 20V, 40V and 57.5V when voltage was applied on only one parallel capacitor drive electrode. As expected, the capacitor electrodes move closer when the voltage increases.

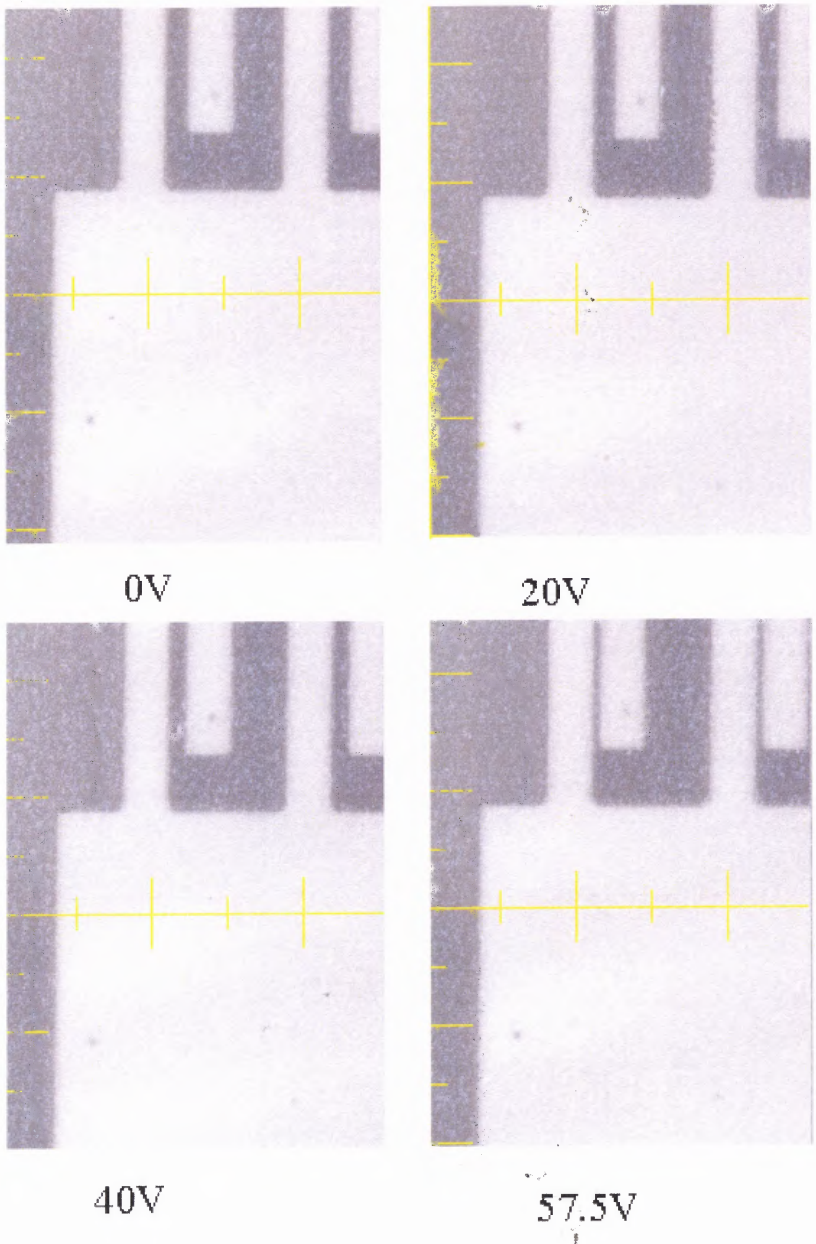

Figure 4.8 A portion of the sense capacitor at various drive voltages with parallel capacitor drive.

Figure 4.9 shows the measured sense capacitance value C_{s1} between one sense electrode E_{s1}, and the common electrode, E_p, with parallel plate capacitor drive. The figure also shows the percentage change in capacitance. The capacitance is measured using an HP 4284A precision LCR meter. The amplitude and frequency of the testing

signal were 5mV and 1MHz, respectively. When voltage is applied on both drive electrodes, the capacitance parabolically increases from 0.945pF at 0V to 3.657pF at 26V, and then increases nearly linearly to 6.57pF at 70V. This corresponds to tuning ranges of 287% at 26V and 595% at 70V. When voltage is applied on one drive electrode, the capacitance increases parabolically from 0.945pF at 0V to 3.696pF at 37.1V, and then nearly linearly to 5.55pF at 75.1V. This corresponds to tuning ranges of 290% at 37.1V and 497.5% at 75.1V. For each measurement, the results are reproducible and without discernable DC hysteresis. In addition, the final displacement appears only to be limited by dielectric breakdown, which exceeds 80V for these devices in air. Comparing the measured capacitance with the designed sense capacitance of 1.36pF at 0V, the experimental value of 0.945pF at 0V is smaller. This result is attributed to wider than expected air gaps formed using the fabricated process. Because of the use of thick SU-8 photoresist, the parasitic capacitance is negligible.

Table 4.1 provides a comparison of the measured transition voltages to analytical and COVENTOR 2001 pull-in simulation results for parallel plate capacitor drive. For completeness, COVENTOR simulation parameters are also given in the table. Good agreement is found for the two cases, when voltage is applied either to only one or to both drive electrodes. Note that the measured transition voltage is slightly higher than the analytical and simulation results, but this can easily be attributed to non-parallel electrodes or other effects neglected in the theory. The possibility of non-parallel electrodes (i.e., a few degree DRIE sidewall slope) is suggested by the observation that the drive electrodes never seem to make full contact at the top surface of the device. While a wide tuning range is achieved in these capacitors, the measured Q factor is

smaller than 100 at 1MHz even with the addition of aluminum. This is attributed to the use of relatively high resistivity, 1–10 Ω·cm, ultra-thin silicon wafers. Even using more heavily doped ultra-thin silicon wafers, with resistivity of 0.01-0.02 Ω·cm, the Q factor is still only ~ 120. Improvements are expected for these devices if they are made using completely metallized electrodes for high Q, and with softer springs and improved drive electrodes to lower the drive voltage.

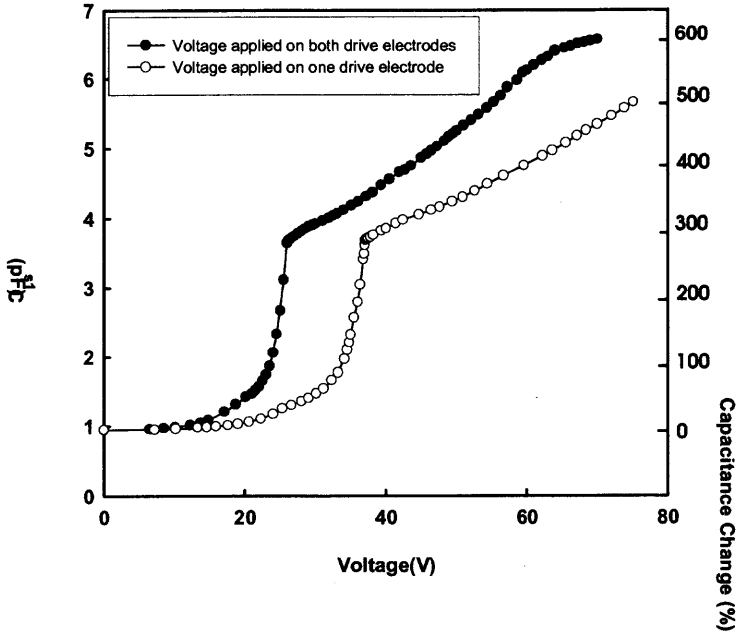

Figure 4.9 The measured sense capacitance C_{s1}, for a parallel plate drive device, measured between E_{s1} and E_p (left axis) and the related percentage change in capacitance (right axis) versus voltage.

Table 4.1 Comparison of measured transition voltage to analytical and COVENTOR simulation results

	Measured transition voltage	Calculated pull-in voltage	COVENTOR pull-in voltage
Voltage on one electrode	37.1V	35.0V	34.25V
			27 node element for meshing 20583 total nodes convergence ratio = 5×10^{-3}
Voltage on both electrodes	26.0V	24.75V	23.91V
			27 node element for meshing 22869 total nodes convergence ratio = 5×10^{-3}

Figure 4.10 shows the measured sense capacitance value C_{s1c} between one sense electrode E_{s1}, and the common electrode, E_p, using the comb capacitor drive device. The figure also shows the percentage change in capacitance. The amplitude and frequency of the testing signal were 5mV and 1MHz, respectively. In this measurement, the drive voltage is applied on both sets of comb drive electrodes. In the figure, the capacitance initially increases parabolically from 0.98pF at 0V to 2.99pF at 22.6V, and then it increases nearly linearly to 3.35pF at 24.8V. Note that the voltage required to achieve roughly a 200% capacitance change, 22.6V, is larger than the design value of 14V. This discrepancy can be attributed to over-etched comb drive features formed during fabrication. In Figure 4.5 notice that while the gap spacing and finger width are designed to be equal to each other, $d_c=w_c=3\mu m$, the measured values are $d_c\approx4\mu m$ and $w_c\approx2\mu m$. Actually, this level of agreement with theory is not bad considering the fact that Equation

4.4 is expected to be valid for $l_c >> d_c$, w_c, h_c, which is not the case in this device. The designed comb drive capacitance is 1.68pF, which compares favorably to the measured value of about 2pF. Similar to the parallel plate drive, the Q factor for the comb drive device is smaller than 100 at 1MHz.

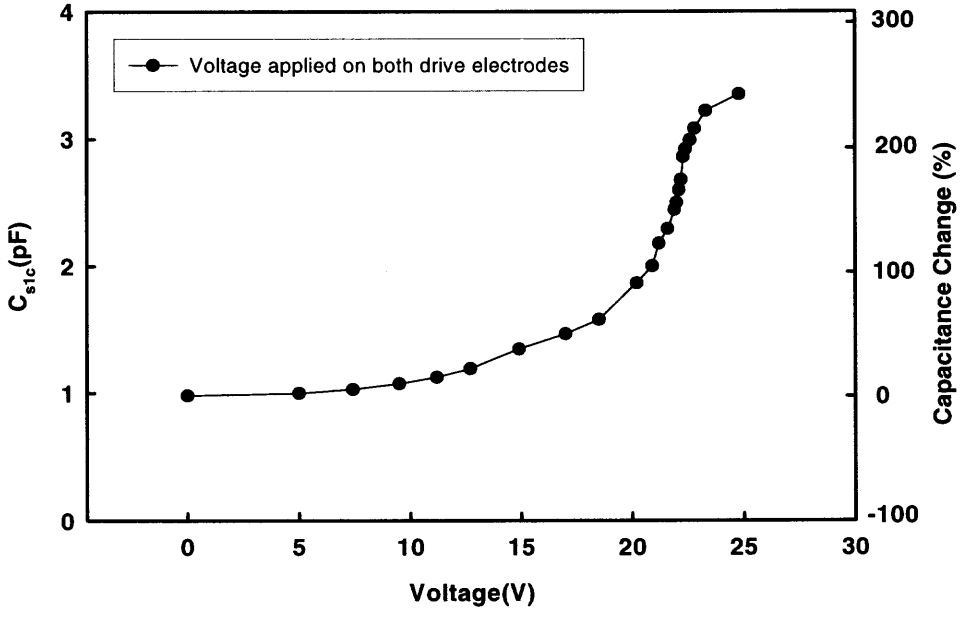

Figure 4.10 The measured sense capacitance C_{s1c} for a comb drive device, measured between E_{s1} and E_p, (left axis) and the related percentage change in capacitance (right axis) versus voltage.

4.3 Summary

In summary, combining ultra-thin silicon wafers, SU-8 bonding and DRIE, a micromachined variable capacitor with parallel plate capacitor drive have been designed and fabricated, which exhibits two tuning regimes: parabolic and linear, and has achieved roughly a 600% tuning range. In addition, a variable capacitor with comb capacitor drive that shows similar performance and has achieved roughly 240% tuning range has been demonstrated.

CHAPTER 5

CONCLUSIONS

First, this thesis has presented a detailed study and analysis of thermal bimorph cantilevers for better understanding of the relationships between performance and design parameters. Optimization for deflection is performed for two bimorph cantilever types: a) with a constant total thickness or b) with one constant and one variable layer thickness. Optimum deflection equations are derived for each case. A good agreement is found between calculation and simulation results. Technological constraints must also be considered. It is found that in the free convection mode, the losses by convection are not dominant. The largest part of the generated heat is lost by conduction in the silicon. The thermal time constant calculation gives the result that the thermal cut-off frequency goes down with the square of the beam length. Faster response time requires higher thermal diffusivity constants, thus high thermal conductivities and short beams. This is in contrast with the requirements for a low power consumption beam. Depending on the application, a compromise has to be found between low power consumption and short response time. For a given applied power on the beam, the average temperature increases as the beam length increases and the beam thickness decreases. A compromise was found between thermal efficiency and mechanical stability.

For the electrostatic actuators study, this thesis presented a systematic investigation of actuation and pull-in for round, double-gimbaled, electrostatic torsion actuators. It is found that for round plates, the fractional tilt at pull-in is only dependent on the electrode length ratio. For outer ring plates, the fractional deflection at pull-in is

only dependent on the electrode length ratio and the ratio of the inner radius to the outer radius. The fractional tilts at pull-in are approximately equal to 1 (i.e., full actuator travel range) for both the inner round plate and the outer ring when electrode length ratios are equal to 0.44. Calculated pull-in and actuation results are verified by comparison with finite element MEMCAD simulations, with fractional difference found to be smaller than 4% for torsion mode dominant systems. It concludes that the straightforward analytical approach provides a reasonable approximation to the more complex and time-consuming finite element analysis simulation method.

This thesis presented several basic equations to describe rectangular electrostatic torsion actuators, which may give designers a better understanding of their performance. Based on these equations, a straightforward, angle based design approach has been proposed, which can avoid time consuming simulations. The results have been verified by comparing them with analytical calculations and MEMCAD simulations, with fractional difference smaller than 3% for torsion mode dominant actuators. Also, good agreement is found by comparison with the measured behavior of a microfabricated full-plate device.

By combining ultra-thin silicon wafers, SU-8 bonding and DRIE, a micromachined variable capacitor with parallel plate capacitor drive has been designed and fabricated, which exhibits two tuning regimes: parabolic and linear, and has achieved roughly a 600% tuning range. In addition, a variable capacitor with comb capacitor drive that shows similar performance and has achieved roughly 240% tuning range has been demonstrated.

REFERENCES

1. K. Goldman and M. Mechregany, "A novel micromechanical temperature memory sensor", in *Proceedings of Transducers'95*, Stockholm, Sweden, pp. 132-135, 1995.

2. T. Lalinsky, S. Hascik, Z. Mozolova, E. Burian, and M. Drzik, "The improved performance of GaAs micromachined power sensor microsystem", *Sensors and Actuators A*, vol. 76, pp. 241-246, 1999.

3. S. Schweizer, P. Cousseau, G. Lammel, S. Calmes, and P. Renaud, "Two-dimensional thermally actuated optical microporjector", *Sensors and Actuators A*, vol. 85, pp. 424-429, 2000.

4. S. Schweizer, S. Calmes, M. Laudon, and P. Renaud, "Thermally actuated optical microscanner with large angle and low comsumption", *Sensors and Actuators A*, vol. 76, pp. 470-477, 1999.

5. J. Buhler, J. Funk, O. Paul, F.-P. Steiner, and H. Baltes, "Thermally actuated CMOS micromirrors", *Sensors and Actuators A*, vol. 46-47, pp. 572-575, 1995.

6. B. Q. Li, J. Lin, and W. Wang, "Thermomechanical deflection of microcantilever beams in scanning force microscopes", *J. Micromech. Microeng.*, vol. 6, pp. 330-336, 1996.

7. T. Lalinsky, E. Burian, M. Drzik, S. Hascik, Z. Mozolova, and J. Kuzmik, "Thermal actuation of a GaAs cantilever beam", *J. Micromech. Microeng.*, vol. 10, pp. 293-298, 2000.

8. Y. Zhang, Y. Zhang, and R. B. Marcus, "Thermally actuated microprobes for a new wafer probe card", *IEEE Journal of microelectromechanical systems*, vol. 8, pp. 43-49, 1999.

9. B. Rashidian and M. G. Allen, "Electrothermal microactuators based on dielectric loss heating", in *Proceedings of MEMS'93*, Fort Lauderdale, FL, pp. 24-29, 1993.

10. I. Jung and Y. Roh, "Design and fabrication of piezoceramic bimorph vibration sensors", *Sensors and Actuators A*, vol. 69, pp. 259-266, 1998.

11. W. Riethmuller and W. Benecke, "Thermally excited silicon microactuators", *IEEE Transactions on Electron Devices*, vol. 35, pp. 758-763, 1988.

12. M. Hoffmann, P. Kopka, and E. Voges, "Bistable micromechanical fibre-optic switches on silicon with thermal actuators", *Sensors and Actuators A*, vol. 78, pp. 28-35, 1999.

13. C. Doring, T. Grauer, J. Marek, M. S. Mettner, H. P. Trah, and M. Willmann, "Micromachined thermoelectrically driven cantilever structures for fluid jet deflection", in *Proceedings of the Micro Electro Mechanical Systems'92*, Travemunde, Germany, pp. 12-18, 1992.

14. X. Q. Sun, K. R. Farmer, and W. N. Carr, "A bistable microrelay based on two segment multimorph cantilever actuators", in *Proceedings of MEMS 98*, Heidelberg, Germany, pp. 154-159, 1998.

15. M. Parameswaran, L. Ristic, K. Chau, A. M. Robinson, and W. Allegretto, "CMOS electrothermal microactuators", in *Proceedings of the 1990 Micro Electro Mechanical Systems*, Napa Valley, CA, pp. 128-131, 1990.

16. D. K. Cheng, *Field and Wave Electromagnetics*, 2nd ed., Addison-Wesley Publishing Company, 1992.

17. W. F. Smith, *Principles of Materials Science and Engineering*, 3rd ed., McGraw-Hill, Inc., 1996.

18. D. Wood, J. S. Burdess, and A. J. Harris, "Actuators and their mechanisms in microengineering", *Engineering Science and Education Journal*, pp. 19-27, 1998.

19. J. M. Gere and S. P. Timoshenko, *Mechanics of Materials*, 4th ed., PWS Publishing Company, 1997.

20. G. Lammel, S. Schweizer, and P. Renaud, *Optical Microscanners and Microspectrometers using Thermal Bimorph Actuators*, Kluwer Academic Publishers, 2002.

21. W. Benecke and W. Riethmuller, "Applications of silicon-microactuators based on bimorph structures", in *Proceedings of the 1989 Micro Electro Mechanical Systems*, Salt Lake City, UT, pp. 116-120, 1989.

22. W. Fang, "Determination of the elastic modulus of thin films materials using self-deformed micro machined cantilevers", *J. Micromech. Microeng.*, vol. 9, pp. 230-235, 1999.

23. W. H. Chu and M. Mehregany, "A study of residual stress distribution through the thickness of p+ silicon films", *IEEE Transactions on Electron Devices*, vol. 40, pp. 1245-1250, 1993.

24. Y. H. Min and Y.-K. Kim, "*In situ* measurement of residual stress in micromachined thin films using a specimen with composite-layered cantilevers", *J. Micromech. Microeng.*, vol. 10, pp. 314-321, 2000.

25. A. S. Jordan and R. Caruso, "Thermal stresses in the bulk and epitaxial growth of III-V materials", *IEEE Transactions on Components, Hybrids, and Manufacturing Technology*, vol. 11, pp. 464-472, 1988.

26. H. Muro, H. Kaneko, S. Kiyota, and P. J. French, "Stress analysis of SiO2/Si bi-metal effect in silicon piezoresistive accelerometers", in *Proceedings of Transducers'91*, San Francisco, CA, pp. 768-771, 1991.

27. J. Funk, J. Buhler, J. G. Korvink, and H. Baltes, "Thermomechanical modeling of an actuated micromirror", *Sensors and Actuators A*, vol. 46-47, pp. 632-636, 1995.

28. D. L. DeVoe and A. P. Pisano, "Modeling and optimal design of piezoelectric cantilever microactuators", *Journal of Microelectromechanical Systems*, vol. 6, pp. 266-270, 1997.

29. Q. Meng, M. Mehregany, and K. Deng, "Modeling of the electromechanical performance of piezoelectric laminated microactuators", *J. Micromech. Microeng.*, vol. 3, pp. 18-23, 1993.

30. R. Watts, M. R. J. Gibbs, W. J. Karl, and H. Szymczak, "Finite-element modeling of magnetostrictive bending of a coated cantilever", *Appl. Phys. Lett.*, vol. 70, pp. 2607-2609, 1997.

31. P. Farber, M. Hormann, M. Bischoff, and H. Kronmuller, "Magnetostrictive bending of an anisotropic free crystal substrate: analytical and numerical solutions", *Journal of Applied Physics*, vol. 85, pp. 7828-7832, 1999.

32. G. A. Gehring, M. D. Cooke, I. S. Gregory, W. J. Karl, and R. Watts, "Cantilever unified theory and optimization for sensors and actuators", *Smart Mater. Struct.*, vol. 9, pp. 918-931, 2000.

33. A. Kruusing, "Analysis and optimization of loaded cantilever beam microactuators", *Smart Mater. Struct.*, vol. 9, pp. 186-196, 2000.

34. W. Peng, Z. Xiao, and K. R. Farmer, "Optimization of thermally actuated bimorph cantilevers for maximum deflection", in *Proceedings of 2003'Nanotech*, San Francisco, CA, USA, vol. 1, pp. 376-379, 2003.

35. W. H. Chu, M. Mehregany, and R. L. Mullen, "Analysis of tip deflection and force of a bimetallic cantilever microactuator", *J. Micromech. Microeng.*, vol. 3, pp. 4-7, 1993.

36. http://www.memsnet.org/material/, 2004.

37. http://www.efunda.com/materials/elements/periodic_table.cfm, 2004.

38. http://www.webelements.com/, 2004.

39. H. E. Salzer, C. H. Richards, and I. Arsham, *Table for the Solution of Cubic Equations*, McGraw-Hill Book Company, 1958.

40. M. Ohring, *The Materials Science of Thin Films*, Academic Press Inc., 1992.

41. S. Wolf and R. N. Tauber, *Silicon Processing for the VLSI Era*, vol. 1, Lattice Press, 1987.

42. F. P. Incropera and D. P. DeWitt, *Fundamentals of heat and mass transfer*, 5th ed., John Wiley & Sons, New York, 2001.

43. J. Soderkvist, "Similarities between piezoelectric, thermal and other internal means of excitating vibrations", *J. Micromech. Microeng.*, vol. 3, pp. 24-31, 1993.

44. T. S. L. Lammerink, M. Elwenspoek, and J. H. J. Fluitman, "Thermal actuation of clamped silicon microbeams", *Sensors and Materials*, vol. 3, pp. 271-238, 1992.

45. H. Sehr, I. S. Tomlin, B. Huang, S. P. Beeby, A. G. R. Evans, A. Brunnschweiler, G. J. Ensell, C. G. J. Schabmueller, and T. E. G. Niblock, "Time constant and lateral resonances of thermal vertical bimorph actuators", *J. Micromech. Microeng.*, vol. 12, pp. 410-413, 2002.

46. Y. C. Ku, *Deflection of Beams for All Spans and Cross Sections*, McGraw-Hill Book Company, 1986.

47. K. Y. Yasumura, T. D. Stowe, E. M. Chow, T. Pfafman, T. W. Kenny, B. C. Stipe, and D. Rugar, "Quality factors in micro- and submicro-thick cantilevers", *Journal of Microelectromechanical Systems*, vol. 9; pp. 117-125, 2000.

48. M. Madou, *Fundamentals of Microfabrication*, CRC Press, 1997.

49. K. E. Petersen, "Silicon as a Mechanical Material", *Proceedings of the IEEE*, vol. 70, pp. 420-457, 1982.

50. K. R. Williams and R. S. Muller, "Etch Rates for Micromachining Processing", *Journal of Microelectromechanical Systems*, vol. 5, pp. 256-269, 1996.

51. J. M. Noworolski, E. H. Klaassen, J. R. Logan, K. E. Petersen, and N. I. Maluf, "Process for in-plane and out-of-plane single-crystal-silicon thermal microactuators", *Sensors and Actuators A*, vol. 55, pp. 65-69, 1996.

52. H. Sehr, A. G. R. Evans, A. Brunnschweiler, G. J. Ensell, and T. E. G. Niblock, "Fabrication and test of thermal vertical bimorph actuators for movement in the wafer plane", *J. Micromech. Microeng.*, vol. 11, pp. 306-310, 2001.

53. J. O'Brien, P. J. Hughes, M. Brunet, B. O'Neill, J. Alderman, B. Lane, A. O'Riordan, and C. O'Driscoll, "Advanced photoresist technologies for Microsystems", *J. Micromech. Microeng.*, vol. 11, pp. 353-358, 2001.

54. D. R. Ciarlo, "A latching accelerometer fabricated by the anisotropic etching of (110) oriented silicon wafer", *J. Micromech. Microeng.*, vol. 2, pp. 10-13, 1992.

55. W. A. Johnson and L. K. Warne, "Electrophysics of micromechanical comb actuators", *Journal of Microelectromechanical Systems*, vol. 4, pp. 49-59, 1995.

56. W. C. Tang, T.-C. H. Nguyen, and R. T. Howe, "Laterally driven polysilicon resonant microstructures", in *Proceedings of the 1989 Micro Electro Mechanical Systems*, Salt Lake City, UT, pp. 53-59, 1989.

57. C. J. Morris and F. K. Forster, "Optimization of a circular piezoelectric bimorph for a micropump driver", *J. Micromech. Microeng.*, vol. 10, pp. 459-465, 2000.

58. M. Dumitrescu, C. Cobianu, and A. Pascu, "Determination of mechanical-thermal deformation in the surface micromachined membrane of the gas microsensors", in *Proceedings of the 2000 Semiconductor Conference*, Sinaia, Romania, vol. 2, pp. 463-466, 2000.

59. R. Puers, A. Cozma, and D. D. Bruyker, "On the mechanisms in thermally actuated composite diaphragms", *Sensors and Actuators A*, vol. 67, pp. 13-17, 1998.

60. A. C. Lapadatu, D. D. Bruyker, H. Jakobsen, and R. Puers, "A new concept for a self-testable pressure sensor based on the bimetal effect", *Sensors and Actuators A*, vol. 82, pp. 69-73, 2000.

61. C. Hsu and W. Hsu, "A two-way membrane-type micro-actuator with continuous deflections", *J. Micromech. Microeng.*, vol. 10, pp. 387-394, 2000.

62. Q. Zou, U. Sridhar, and R. Lin, "A study on micromachined bimetallic actuation", *Sensors and Actuators A*, vol. 78, pp. 212-219, 1999.

63. J. A. Walker, "The future of MEMS in telecommunications networks", *J. Micromech. Microeng.*, vol. 10, R1-R7, 2000.

64. J. Buhler, J. Funk, J. G. Korvink, F. P. Steiner, P. M. Sarro, and H. Baltes, "Electrostatic aluminum micromirrors using double-pass metallization", *Journal of Microelectromechanical Systems*, vol. 6, pp. 126-135, 1997.

65. H. Toshiyoshi and H. Fujita, "Electrostatic micro torsion mirrors for an optical switch matrix", *Journal of Microelectromechanical Systems*, vol. 5, pp. 231-237, 1996.

66. S. W. Chung, J. W. Shin, Y. K. Kim, and B. S. Han, "Design and fabrication of micromirror supported by electroplated nickel posts", *Sensors Actuators A*, vol.54, pp. 464-467, 1996.

67. Y. Uenishi, M. Tsugai, and M. Mehregany, "Micro-opto-mechanical devices fabricated by anisotropic etching of (110) silicon", in *Proceedings of MEMS'94*, Oiso, Japan, pp. 319-324, 1994.

68. M. Fischer, M. Giousouf, J. Schaepperle, D. Eichner, M. Weinmann, W. von Munch, and F. Assmus, "Electrostatically deflectable polysilicon micromirrors-Dynamic behavior and comparison with results from FEM modeling with ANSYS", *Sensors Actuators A*, vol. 67, pp. 89-95, 1998.

69. L. J. Hornbeck, "Deformable-mirror spatial light modulators", *SPIE Critical Review Series 1150 Spatial Light Modulators and applications*, pp. 86-102, 1989.

70. P. M. Osterberg, "Electrostatically actuated micromechanical test structures for material property measurements", *Ph.D dissertation, Dept. Elec. Eng. Comput. Sci., Massachusetts Institute of Technology*, 1995.

71. R. K. Gupta, "Electrostatic pull-in test design for in-situ mechanical property measurements of microelectromechanical systems (MEMS)", *Ph.D dissertation, Dept. Elec. Eng. Comput. Sci., Massachusetts Institute of Technology*, 1997.

72. O. Degani, E. Socher, A. Lipson, T. Leitner, D. J. Setter, S. Kaldor, and Y. Nemirovsky, "Pull-in study of an electrostatic torsion microactuator", *IEEE J. Microelectromech. Syst.*, vol. 7, pp. 373-379, 1998.

73. "MEMCAD is a finite element MEMS design tool available from Coventor, Inc.", 4001 Weston Parkway, Cary, NC 27513, USA.

74. Z. Xiao, X. Wu, W. Peng, and K. R. Farmer, "An angle based design approach for rectangular electrostatic torsion actuators", *IEEE J. Microelectromech. Syst.*, vol.10, pp. 561-568, 2001.

75. S. P. Timoshenko and I. N. Goodier, *Theory of Elasticity*, McGraw-Hill, 1970.

76. R. S. Muller and T. I. Kamins, *Device electronics for integrated circuits*, John Wiley & Sons Inc., 1977.

77. F. Svelto, P. Erratico, S. Manzini, and R. Castello, "A metal-oxide-semiconductor varactor", *IEEE Electron Device Letters*, vol. 20, pp. 164-166, 1999.

78. C. L. Goldsmith, A. Malczewski, Z. J. Yao, S. Chen, J. Ehmke, and D. H. Hinzel, "RF MEMS variable capacitors for tunable filters", *International Journal of RF and Microwave Aided Engineering*, vol. 9, pp. 362-374, 1999.

79. D. J. Young, V. Malba, J. J. Ou, A. F. Bernhardt, and B. E. Boser, "Monolithic high-performance three–dimensional coil inductors for wireless communication application", *Tech. Digest, International Electron Devices Meeting*, pp. 67-70, 1997.

80. D. J. Young, V. Malba, J. T. Ou, A. F. Bernhardt, and B. E. Boser, "A low-noise RF voltage-controlled oscillator using on-chip high Q three-dimensional coil inductor and micromachined variable capacitor", *Technical Digest of Solid-State Sensor and Actuator Workshop*, Hilton Head Isl., SC, USA, pp. 128-131, 1998.

81. D. J. Young and W. E. Boser, "A micromachined variable capacitor for monolithic low-noise VCOs in cellular phone application", *Technical Digest of Solid-State Sensor and Actuator Workshop*, Hilton Head Isl., SC, USA, pp.86-89, 1996

82. M. Steyaert and J. Craninckx, "1.1 GHz oscillator using bondwire inductance", *Electronics Letters*, vol.30, pp.244-245, 1994.

83. D. J. Young, J. L. Tham, and B. E. Boser, "A micromachine-based low phase-noise GHz voltage-controlled oscillator for wireless communications", in *Proceeding of 10th Solid-State Sensor and Actuators*, Sendai, Japan, pp.1386-1389, 1994.

84. A. Dec and K. Suyama, "Micromachined varactor with wide tuning range", *Electronics Letters*, vol.33, pp.922-924, 1997.

85. A. Dec and K. Suyama, "A 1.9GHz micromachined-based low phase noise CMOS VCO", in *Proceeding of 46th IEEE International Solid-State Circuits Conference*, San Francisco, CA, USA, pp. 80-81, 1999.

86. E. S. Hung and S. D. Senturia, "Tunable capacitors with programmable capacitance-voltage characteristic", *Technical Digest of 1998 Solid-State Sensor and Actuator Workshop*, Hilton Head Isl., SC, USA, pp. 292-295, 1998.

87. M. Husák, "One-chip integrated resonance circuit with a capacitive pressure sensor", *J. Micromech. Microeng.*, vol.7, pp.173-178, 1997.

88. J. J. Yao, "RF MEMS from a device perspective", *J. Micromech. Microeng.*, vol.10, R9-R38, 2000.

89. A. Dec and K. Suyama, "Microwave MEMS-Based Voltage-Controlled Oscillators", *IEEE Transactions on Microwave Theory and Techniques*, vol.48, pp.1943-1949, 2000.

90. J. Zou, C. Liu, J. Schutt-Aine, J. Chen, and S. M. Kang, "Development of Wide Tuning Range MEMS Tunable Capacitor for Wireless Communication Systems",

Tech. Digest, International Electron Devices Meeting, San Francisco, CA, USA, pp.403-406, 2000.

91. Z. Feng, H. Zhang, W. Zhang, B. Su, K. Gupta, V. Bright, Y. Lee, "MEMS-based variable capacitor for millimeter-wave applications", *Tech. Digest, Solid-State sensors and Actuators Workshop*, Hilton Head Island, SC, USA, pp.255-258, 2000.

92. R. L. Borwick III, P. A. Stupar, J. DeNatale, R. Anderson, C. Tsai, and K. Garrett, in *Proceedings of 15th IEEE International Microelectromechanical Systems*, Las Vegas, Nevada, USA, pp. 669-672, 2002.

93. R. Legtenberg, J. Gilbert, S. D. Senturia, and M. Elwenspoek, "Electrostatic curved electrode actuators", *IEEE J. of Microelecromechanical Systems*, vol.6, pp.257, 1997.

94. W. A. Johnson and L. K. Warne, "Electrophysics of micromechanical comb actuators", *IEEE Journal of Microelectromechanical Systems*, vol.4, pp.49-59, 1995.

95. M. R. Boyd, S. B. Crary, and M. D. Giles, "A heuristic approach to the electromechanical modeling of MEMS beams", in *Proceedings of IEEE Solid-State Sensor and Actuator Workshop*, Hilton Head Island, SC, USA, 1994.

96. B. P. van Drieenhuizen, "Integrated Electrostatic RMS-to-DC Converter, Fabricated in a BIFET-compatible surface-micromachining process", *Ph.D dissertation, Delft University of Technology*, The Netherlands, 1996.

97. "Ultrathin silicon wafers are available from Virginia Semiconductor, Inc.", Fredericksburg, VA, USA.

98. S. K. Sampath, L. St.Clair, X. Wu, D. V. Ivanov, Q. Wang, C. Ghosh, and K. R. Farmer, "Rapid MEMS Prototyping using SU-8, Wafer Bonding and Deep Reactive Ion Etching", in *Proceedings of the 13th Biennial University/Government/Industry Microelectronics Symposium*, Richmond, VA, USA, pp.158-161, 2001.

99. R. A. Brown, V. Aksyuk, and K. R. Farmer, "Micromachined, electrostatically-actuated optical modulators fabricated by fusion bonding of single-crystal, ultra-thin silicon wafers", in *Proceedings of the 5th International Symposium on Semiconductor Wafer Bonding: Science, Technology and Applications,* Honolulu, Hawaii, pp.407-410, 1999.